International Journal of Mechanical Sciences 312 (2026) 111247

Contents lists available at ScienceDirect

International Journal of Mechanical Sciences

journal homepage: www.elsevier.com/locate/ijmecsci

Atomic-scale damage mechanism of diamond during laser processing

Song Yuan [a], Wanxue Zhang [b], Chi Fai Cheung [a,*], Qixian Zhang [a], Ze Li [a], Chunjin Wang [a,*]

[a] State Key Laboratory of Ultra-precision Machining Technology, Department of Industrial and Systems Engineering, The Hong Kong Polytechnic University, Hong Kong, China

[b] State Key Laboratory of High-performance Precision Manufacturing, School of Mechanical Engineering, Dalian University of Technology, Dalian, China

ARTICLE INFO

Keywords:
Laser processing
Molecular dynamics simulations
Damage mechanism
Diamond
Anisotropy
Energy density

ABSTRACT

Laser processing is widely used for diamond machining, yet its atomic-scale damage mechanisms remain unclear due to the complex interactions between laser and diamond. In this work, femtosecond laser experiments and molecular dynamics (MD) simulations were combined to elucidate the atomic-scale damage mechanisms of diamond during laser processing. Laser experiments reveal that multi-pulse irradiation leads to deep ablation crater, while single-pulse laser irradiation induces surface bulging, with damage characteristics strongly dependent on the energy density. The detailed analysis of the surface morphologies and subsurface structures were provided, identifying distinct bulging–swelling–melting and recasting–laser induced periodic surface structure (LIPSS) formation pathways linked to energy density. Complementary MD simulations resolve the transient evolution of temperature, stress fields, and local bonding configurations, reproducing the experimental observations and uncovering a coupled thermo-stress-phase transition mechanism that drives the structural transformation of diamond. Notably, crystal orientation is found to play a crucial role in modulating the damage propagation and material removal mechanisms. The (111) crystal plane exhibits unique atomic-layer exfoliation, while the (100) and (110) planes show more rapid stress expansion and surface deformation. The study establishes a mechanistic map linking energy density, crystal orientation, and damage mode and offers critical insights for tailoring laser parameters during laser processing of diamond.

1. Introduction

Diamond, often hailed as the "ultimate semiconductor material" due to its ultra-wide bandgap, exceptional thermal conductivity, outstanding carrier mobility, and high breakdown field, shows tremendous potential for high-performance chips, quantum information devices [1], and high-power optoelectronic components [2–4]. However, its extreme hardness and chemical inertness make diamond notoriously difficult to process [5]. Conventional approaches, including mechanical polishing [6–11], chemical mechanical polishing (CMP) [12–15], UV-assisted CMP [16–19], plasma polishing [20–23], plasma-assisted polishing [24–27], and dynamic friction polishing [28–31], can improve surface finish but suffer from low efficiency and long processing cycles [32].

Laser processing has emerged as a promising approach for efficient processing of hard and brittle materials [33–35] and preparing microstructure [36] owing to its unique optical and thermal interactions with matter, which enable high material removal rates while minimizing mechanically induced damage [37–40]. The interaction between laser irradiation and diamond involves highly complex physicochemical processes. Once the surface temperature exceeds ~700 °C, diamond, a metastable carbon phase, tends to spontaneously transform into graphite accompanied by ablation [41], sublimation [42,43], resolidification [44], graphitization [45], and phase transitions [46,47]. Typically, material removal proceeds through surface graphitization followed by graphite sublimation [48], enabling rapid multi-micrometer-scale removal and substantial surface roughness reduction after repeated scanning [49].

However, nanosecond pulsed lasers often introduce significant thermal accumulation, resulting in dislocations, cracks, and even catastrophic fracture [50,51]. At high energy densities, non-uniform temperature fields and thermal stresses aggravate crack propagation, while surface morphology is further influenced by parameters such as incidence angle and scanning speed [52]. The damage features after

* Corresponding authors.
E-mail addresses: Benny.Cheung@polyu.edu.hk (C.F. Cheung), chunjin.wang@polyu.edu.hk (C. Wang).

https://doi.org/10.1016/j.ijmecsci.2026.111247
Received 10 November 2025; Received in revised form 22 December 2025; Accepted 11 January 2026
Available online 12 January 2026

nanosecond pulsed laser ablation generally include cracks, grooves, ripples, and debris deposition [53]. Studies have shown that laser reflections at groove walls promote ripple formation, while plasma absorption leads to groove deformation, and ablation debris consists of spherical graphite particles or irregular diamond fragments [54]. Furthermore, Yan et al. [55] demonstrated that nanosecond pulsed lasers induce instantaneous sp^3-to-sp^2 transformation in diamond, enabling subsequent mechanical cleavage and even graphene formation. In addition, coating-based strategies (e.g., metal or carbon layers) have been employed to enhance laser energy absorption and suppress subsurface damage [56,57]. For instance, titanium and gold coatings can significantly reduce ablation thresholds and post-processing roughness [44], while Liu et al. [58] proposed a Metal Film-Induced Self-Sustaining Graphitization technique to improve ablation efficiency with reduced subsurface damage.

Compared with nanosecond lasers, ultrashort pulsed lasers (picosecond/ femtosecond) offer distinct advantages due to their pulse durations being shorter than the mean atomic collision time. This suppresses heat diffusion and minimizes macroscopic heat-affected zones, thus enabling "cold processing" with high-quality surface modification. Picosecond lasers combine ultrashort pulse widths ($<10^{-12}$ s) with high peak power densities, achieving precise micromachining of diamond with negligible peripheral cracking [59]. However, their material removal rates are significantly lower than those of nanosecond lasers, which remain more suitable for large-scale cutting or fabrication of high-aspect-ratio structures [60]. In contrast, picosecond lasers are better suited for high-precision processing where minimal thermal damage and smooth surface finish are required. Based on Gaussian beam theory, Zhai et al. [61] explore the effects of the laser parameters on the surface characteristics of diamond, the thermal affected zone that causes deterioration of the diamond surface during laser processing can be revealed by establishing the temperature field, thermal stress field and phase field through simulation. Subsequent studies [62] confirmed that picosecond pulsed lasers markedly reduce surface roughness of polycrystalline diamond (PCD), suppress graphite formation, and highlight the effects of crystal orientation and pulse number on groove morphology and phase transformations. Yan et al. [63] developed a physics-based surface morphology model for picosecond laser processing. The model quantitatively predicts the surface roughness and material removal depth of diamond, with average relative errors of 9.6 % and 16.6 %, respectively. Okamoto et al. [64] found that cleavage is observed along the (111) planes parallel to the crystal orientation during laser processing of diamond, while some graphite formation may occur, the diamond crystal structure remains largely intact.

Femtosecond lasers provide an even more localized ablation regime, where energy deposition is confined to the near-surface region, thus avoiding extensive thermal diffusion. They enable fabrication of micro/ nanoscale structures with minimal residual stress [65,66]. Phase transitions under femtosecond irradiation are complex, including the formation of diaphite, amorphous carbon, nanocrystalline graphite, and even transient diamond–graphite–graphene composites [67,68]. Experimental results indicate that by tuning pulse energy and scanning speed, femtosecond lasers can induce sequential removal stages—melting, graphitization, and sublimation—while surface roughness and removal efficiency are strongly dependent on processing parameters [69].

The interaction between ultrafast laser and diamond is inherently nonlinear, non-equilibrium, and orientation-dependent [70,71]. Yet, the atomic-scale dynamic structural evolution during this process remains poorly understood. Elucidating these mechanisms is essential for predicting subsurface defects and optimizing processing strategies [72]. While finite element modeling has provided valuable insights into surface morphology evolution and temperature field distributions during laser ablation [61,73], such continuum-scale models cannot capture ultrafast, non-equilibrium energy transport, defect nucleation, and phase-transition mechanisms at the nanoscale. As processing advances toward the atomic scale, manufacturing involves direct atomic-level interactions [74], necessitating a detailed understanding of temperature evolution, stress-wave dynamics, and phase transformation mechanisms during ultrafast laser ablation. Molecular dynamics (MD) simulations have recently emerged as a powerful tool to investigate ultrafast laser-induced material removal and phase transitions at the nanoscale [75–80]. They have been applied to study interfacial structural changes [81,82], temperature and stress evolution [83,84], lattice transformations, and mechanical property alterations [85], as well as stress-wave generation [86], surface graphitization [87,88] and heterogeneous grain-boundary removal [75], brittle-to-ductile transition mechanism during nano-grinding [89,90]. These efforts have significantly advanced our understanding of nanoscale damage mechanisms.

Despite the widespread use of laser processing in diamond, the underlying mechanisms of damage formation remain poorly understood, primarily due to the intricate and complex interplay between thermal, mechanical, and structural effects during ultrafast laser irradiation. While previous studies have provided valuable insights into surface morphologies and phase transitions, a detailed understanding of the atomic-scale dynamics, including stress evolution, temperature distribution, and material removal mechanisms, is still lacking. Furthermore, the role of crystal orientation in modulating these processes remains inadequately explored.

In summary, although previous studies have explored laser-induced surface modification of diamond, the fundamental coupling mechanisms linking temperature evolution, stress development, and subsequent structural transitions remain insufficiently resolved. To address this gap, this work combines systematic ultrafast laser experiments with MD simulations to reveal the multiscale response of diamond under different irradiation conditions. By investigating the effects of energy density, pulse number, and crystal orientation, we provide new insights into how these factors govern damage modes and material removal. The integrated framework enables direct correlation between ablation morphology, phase evolution, and atomistic dynamics. The major contributions of this study are: (i) establishing a unified experimental–simulation correlation strategy for characterizing damage evolution in diamond under ultrafast laser irradiation; (ii) uncovering the causal linkage among transient thermal spike, stress redistribution, and sp^3–to–sp^2 bonding transition; and (iii) elucidating crystal-orientation–dependent removal modes and structural reconstruction pathways. This framework will be crucial for tailoring laser parameters in precision machining applications, as it reveals how energy density and crystal orientation together shape the laser-diamond interaction and material response.

The paper is organized as follows. Section 2 describes the methodology, including the experimental setup and computational framework. Section 3.1 provides a detailed analysis of the surface morphology resulting from laser experiments. Section 3.2 investigates the atomic-scale damage mechanisms driven by energy density using MD simulations, with results validated through TEM characterization. Section 3.3 examines the atomic damage mechanisms influenced by crystal orientation, also using MD simulations and validated by TEM observations. Finally, Section 4 presents the conclusions, summarizing the key insights obtained from the integration of experimental and computational approaches and providing guidance for optimizing laser parameters in precision machining of superhard materials.

2. Methodology

This section presents a detailed description of both the experimental and computational methods. Section 2.1 outlines the experimental setup, including the configuration of the femtosecond laser system, pulse energy and repetition rate settings, as well as the preparation of single-crystal diamond samples and the employed surface characterization techniques. Section 2.2 describes the MD simulation framework, emphasizing the crystal orientation, laser energy deposition process,

and relevant computational parameters.

2.1. Experimental setup

The femtosecond laser experiments were conducted using a Yb: KGW-based femtosecond laser system (PHAROS), which provides adjustable pulse duration and precise control over the number of emitted pulses. The laser equipment for diamond is shown in Fig. 1(a). After beam expansion and collimation, the laser pulses were focused onto the diamond surface through a high-numerical-aperture microscope objective, the schematic of laser processing diamond is shown in Fig. 1(b). The workpiece material was (100)-oriented single-crystal diamond with an initial surface roughness of Ra $<$ 1 nm, as measured prior to irradiation. Before and after processing, the sample surfaces were cleaned with ethanol to remove potential contaminants.

The diamond specimens were mounted on a motorized translation stage to ensure accurate positioning and repeatable exposure. The laser repetition rate was fixed at 50 kHz, with a pulse duration of 1 ps. For the multi-pulse experiments, two pulse energies (2 μJ and 16 μJ) were employed, with pulse numbers set to 20, 50, and 80, respectively. For the single-pulse experiments, eight energy levels were investigated, ranging from 2 μJ to 16 μJ in a stepwise gradient of approximately 2 μJ. Following irradiation, the surface morphology and structural modifications were characterized using Raman spectroscopy, scanning electron microscope (SEM), Raman spectroscopy, atomic force microscope (AFM), and transmission electron microscope (TEM) to correlate surface topography with phase transformation and damage evolution.

2.2. Computational setup

In this study, large-scale atomic/molecular parallel simulator (LAMMPS) [91,92] was employed for MD simulations, and all visualization and post-processing analyses were performed using open visualization tool (OVITO) [93]. The simulation systems consisted of single crystal diamond blocks subjected to ultrafast laser energy deposition. Three crystal orientation, namely (100), (110), and (111), were constructed, with lattice dimensions of approximately 15 nm × 15 nm × 20 nm, as shown in Fig. 1(c) and Fig. 1(d). Along the normal direction, a buffer layer with a thickness of 10 lattice constants was added and divided into a thermostat region and a Newton region. The Newton region was used to capture the actual dynamic response of the laser-lattice interaction, while the thermostat region controlled atomic velocities through a Langevin thermostat [94] to mimic heat dissipation into an external reservoir and prevent non-physical temperature accumulation. Prior to laser loading, the systems were relaxed under the NVT ensemble for 10 ps to reach an equilibrium state close to 300 K. The Tersoff

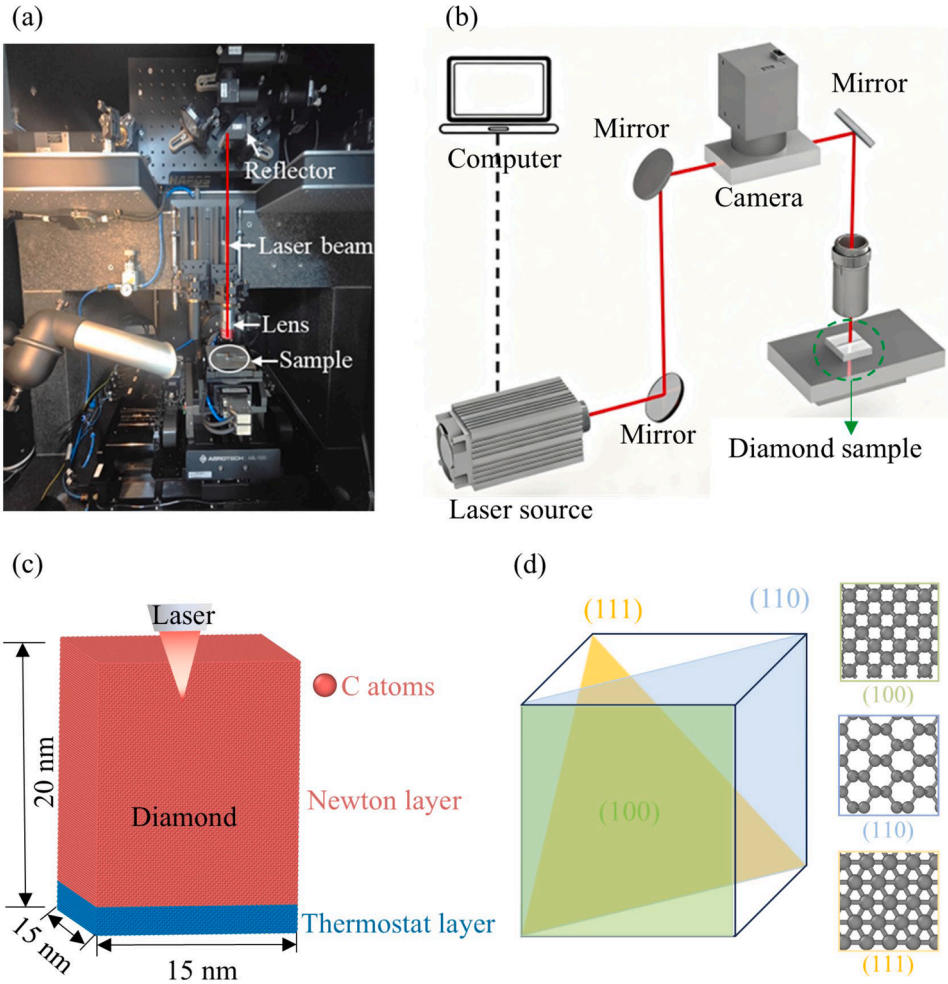

Fig. 1. Laser Equipment Configuration for Diamond Processing and MD Simulation Setup. (a) Laser equipment setup for diamond processing, showing the experimental setup with key components such as the laser beam, lens, reflector, and diamond sample, enabling precise laser treatment on the diamond. (b) Schematic of laser processing diamond, illustrating the laser processing system, including the laser source, mirrors, camera, and the computer-controlled setup for processing the diamond sample. (c) MD model of laser processing diamond, displaying the molecular dynamics model of the laser interaction with the diamond, showing the Newton and thermostat layers simulating atomic dynamics and temperature effects. (d) Schematic of different crystal orientations of diamond showing the atomic arrangements for the (100), (110), and (111) planes of diamond, illustrating how laser interaction varies with crystal orientation.

potential [95] was selected due to its proven ability to accurately describe carbon–carbon bonding behavior, including the hybridization transition between sp^3 and sp^2 structures that is critical during ultrafast laser irradiation. This potential captures the bond-order dependence, anharmonic effects, and many-body interactions required to model structural degradation, phase transition, and recrystallization under high temperature and high-pressure conditions. The equations of motion were integrated using a modified velocity-Verlet algorithm [96], with a time step of 0.1 fs during laser loading and 1 fs during the post-loading relaxation process. During the laser loading stage, a smaller time increment is necessary to resolve the ultrafast atomic motion and strong force fluctuations arising from the intense and highly localized energy deposition, and to maintain numerical stability and energy conservation at temperatures exceeding several thousand Kelvin. The laser parameters of the MD model are given in Table 1.

Ultrafast laser processing involves complex coupling between electronic and lattice subsystems, which is inherently nonlinear and beyond the scope of classical MD. To represent photon energy absorption, the Beer–Lambert model was implemented, which simplifies laser absorption as an exponential decay along the depth direction. The Beer–Lambert law is used as a first-order approximation to represent the spatial attenuation of absorbed laser energy during the ultrafast excitation stage. Although it does not fully describe carrier transport and other non-equilibrium effects, previous studies have demonstrated that it provides a reasonable estimation of energy decay in wide-bandgap materials under femtosecond irradiation [97,98].

The Beer–Lambert describes the attenuation of laser intensity with depth [85]:

$$I(z) = I_o e^{-\alpha z},$$

where I (z) is the laser intensity at depth z, α is the absorption coefficient of diamond (0.1 nm^{-1} [97]), I_0 is the incident laser intensity at the surface. The laser-affected region was discretized into 28 layers along the depth direction, with the absorbed energy in each layer calculated as the difference between adjacent interfaces and uniformly converted into the kinetic energy of atoms in that layer, achieving quasi-continuous energy deposition. A single-pulse laser with a pulse width of 1 ps, pulse interval of 50 ps, spot diameter of 30 nm, and penetration depth of 10 nm was applied, with energy densities ranging from 0.1 to 0.15 J/cm^2.

3. Results and discussion

This section presents a comprehensive analysis of the experimental and simulation results to elucidate the atomic-scale damage mechanisms of diamond under femtosecond laser irradiation. The discussion integrates macroscopic observations from SEM, AFM, and Raman spectroscopy, TEM with atomistic insights obtained from MD simulations. By correlating experimental and computational findings, this section aims to reveal the multiscale coupling between thermal, mechanical, and structural responses during laser–diamond interactions.

Specifically, Section 3.1 examines the surface morphology evolution and phase transformation behavior of diamond under different pulse numbers and energy densities, highlighting the macroscopic manifestations of laser-induced damage. Section 3.2 focuses on the atomic-scale damage mechanisms as a function of energy density, using TEM and MD simulations to resolve transient temperature, stress, and structural evolutions. Section 3.3 further explores the influence of crystal orientation on anisotropic heat transfer, stress propagation, and damage formation, providing fundamental insights into orientation-dependent material removal processes. Together, these analyses establish a multiscale framework linking experimental observations with atomic-level mechanisms to clarify the origins of laser-induced deformation and damage in diamond.

Table 1
Laser parameters of the MD model.

parameters	Values
Crystal orientations	(100), (110), (111)
Laser radius (nm)	3
Size of workpiece (nm)	15 × 15 × 20
Penetration depth of laser (nm)	10
Initial temperature (K)	300
Laser power density (J/cm^2)	0.1, 0.12, 0.15
Laser loading time (ps)	1
Laser unloading time (ps)	50
Timesteps during laser loading (fs)	0.1
Timesteps during laser unloading (fs)	1

3.1. Surface morphology of diamond after laser processing

To optimize laser processing of diamond and improve material removal efficiency, it is crucial to understand how laser parameters like pulse number and energy density influence surface morphology and subsurface damage. This section aims to investigate how varying pulse numbers and energy densities impact diamond's surface morphology, providing insights into energy accumulation, material removal, and surface modification.

Fig. 2 shows representative SEM images of single-spot ablation on diamond under a laser energy of 16 μJ, with varying pulse numbers. Following a single pulse, a surface bulge is observed in the laser-affected region. This bulge signifies localized thermal expansion and structural transformation, indicating that the material undergoes significant heating and initial phase transitions at the laser focus point. As the pulse number increases to 20 pulses, a clear crater begins to form on the surface. At this stage, LIPSS are observed surrounding the crater, signifying a combination of melting and rapid solidification. This suggests that the accumulated energy over multiple pulses is sufficient to induce surface modulation and localized material removal. With further increase into 50 pulses, the ablation pit radius gradually expands. A prominent melting and recasting layer appear, with signs of localized material reflow and redistribution. The surface shows a more pronounced structural change, reflecting enhanced energy absorption and deeper material modification. At this stage of 80 pulses, the damage extends laterally, and surface cracks begin to emerge. The ablation pit deepens, forming an inverted cone shape. Clear signs of material vaporization are visible at the pit's bottom, further indicating that the deposited energy is sufficient to trigger local phase transitions and material removal.

Overall, the results demonstrate that as the pulse number increases, the ablation pit deepens primarily in the vertical direction, with lateral expansion occurring to a lesser extent. This trend underscores the progressive accumulation of laser energy, which leads to a more significant structural transformation, surface modification, and material removal.

To explore the early evolution of laser-induced damage, we conducted additional single-pulse experiments at varying energy densities, as shown in Fig. 3. Unlike the multi-pulse experiments, no LIPSS were observed after a single pulse. At an energy density of 4 μJ, a localized bulging in the center of the laser-affected region was observed, which gradually expanded with increasing energy. This indicates that the initial response of the material is primarily dominated by thermal expansion and volumetric swelling beneath the surface, driven by melting, rather than direct vaporization. In contrast, the formation of LIPSS in multi-pulse experiments results from the periodic redistribution of energy accumulated across successive pulses.

Fig. 4 illustrates the AFM morphologies of diamond after single pulse laser experiments under different energy densities. As seen from Fig. 4, the bulging region continued to grow with the increasement of energies, and the material started expanding outward and upward, suggesting that with each increase in energy, the thermal effects became more pronounced, leading to deeper surface modifications. This process begins with localized heating, causing surface expansion, followed by

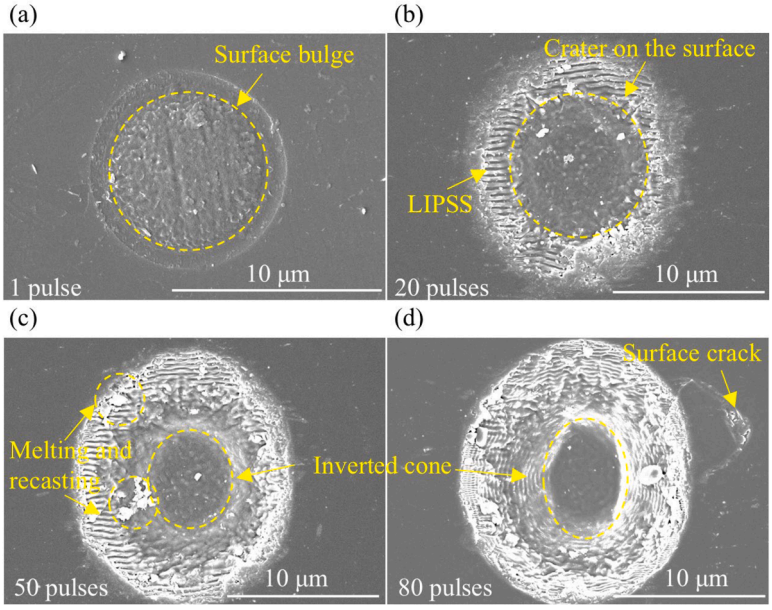

Fig. 2. SEM morphologies of diamond after single-spot ablation under 16 μJ with various pulse numbers. (a) At 1 pulse: This image shows the surface of the diamond after one laser pulse, displaying a surface bulge, indicative of initial material deformation from the laser energy. (b) After 20 pulses, the surface exhibits a crater, with LIPSS formed around the edges of the crater. The periodic surface features indicate the interaction of multiple pulses and the formation of microstructures due to laser energy absorption. (c) After 50 pulses, the surface shows signs of melting and recasting, with a clear inverted cone shape formed in the center. This suggests that the laser energy has been sufficient to cause localized melting and re-solidification, altering the diamond's surface topography. (d) After 80 pulses, a surface crack appears along with the formation of an inverted cone structure. The crack formation indicates significant thermal stress and material weakening from the repeated laser impacts.

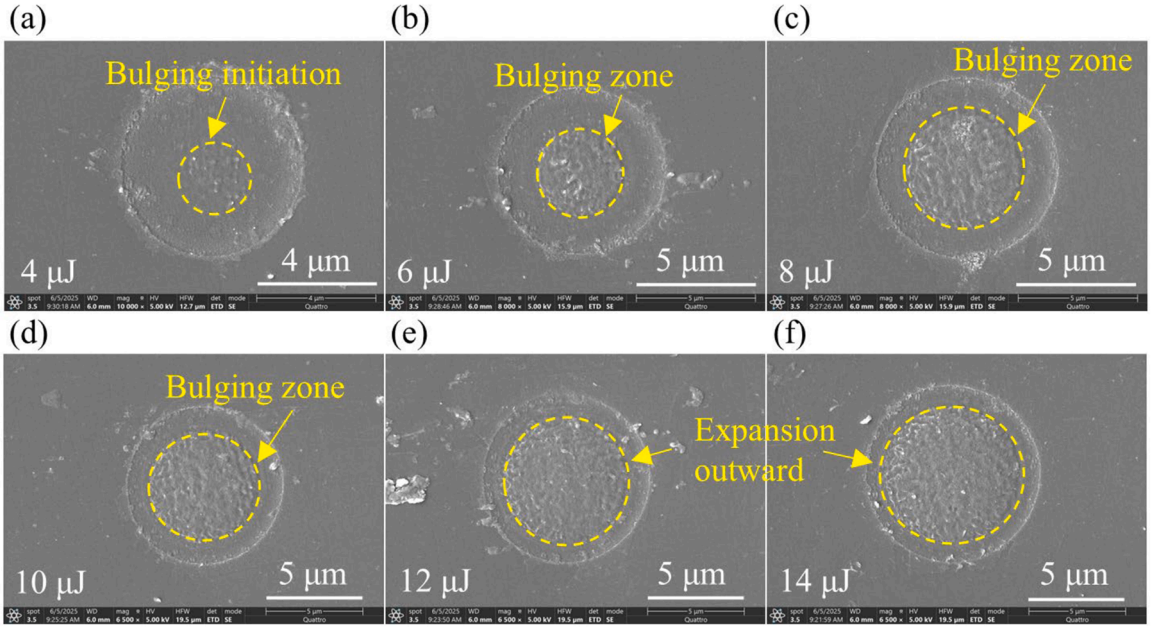

Fig. 3. SEM morphologies of diamond after single-pulse laser experiments under different energy densities. (a) At 4 μJ energy density: This image shows the initiation of bulging on the diamond surface after laser exposure, with a clear, localized deformation indicating the start of material displacement. (b) At 6 μJ energy density: the bulging zone expands further, with more pronounced deformation along the surface, suggesting an increase in material displacement under the laser's impact. (c) At 8 μJ energy density: The bulging zone continues to grow, leading to more significant deformation within the affected area. (d) At 10 μJ energy density: the bulging zone is more defined, indicating a more extensive material response. (e) At 12 μJ energy density: The bulging continues, but now with a visible expansion outward. (f) At 14 μJ energy density: the surface shows significant expansion outward, with clear deformation patterns forming on the diamond surface, demonstrating the full effect of the laser energy.

melting, and ultimately leading to further energy accumulation, where direct vaporization and ejection of carbon atoms occur, deepening the pit into an inverted cone shape.

These findings highlight that LIPSS are not an initial damage feature but rather a secondary surface modulation effect triggered by the accumulation of critical energy over multiple pulses. The single-pulse experiments serve as a baseline to understand the fundamental thermal and mechanical responses of diamond to individual laser impacts,

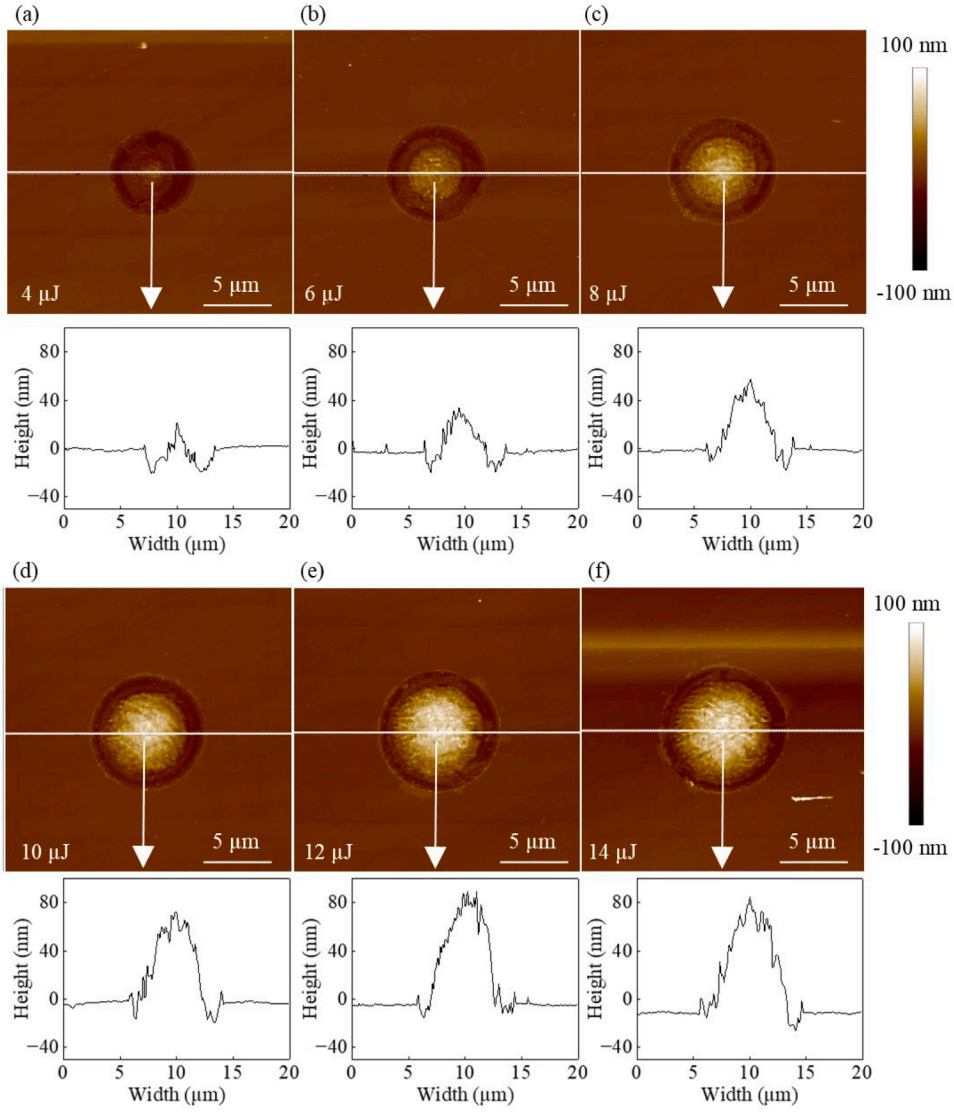

Fig. 4. AFM morphologies of diamond after single-pulse laser experiments under different energy densities. (a) The AFM image shows the surface morphology of diamond after a single pulse with an energy density of 4 μJ, with a slight elevation observed at the center of the laser impact area. (b) At an energy density of 6 μJ, the surface begins to show a more noticeable deformation, with a slight bulge in the center. The height profile reveals increased material displacement compared to the 4 μJ case. (c) At this energy density of 8 μJ, the AFM image shows more pronounced surface deformation with a clearer peak at the center of the laser impact. The height profile indicates an increase in material displacement as the energy density increases. (d) With an energy density of 10 μJ, the AFM image shows a more pronounced surface deformation with a central bulge. The height profile further reflects significant material displacement and the development of a more defined peak in the center. (e) At 12 μJ, the surface of the diamond exhibits more significant deformation, with an increased bulge in the center. The height profile reveals a wider peak and deeper material displacement, indicating the higher energy density's effect. (f) The AFM image at 14 μJ shows a large bulge at the center of the diamond surface, accompanied by substantial material displacement.

shedding light on the initial stages of damage before the more complex effects of multiple pulses become apparent. It enables precise modulation of diamond materials, thereby avoiding the excessive damage that may occur during traditional multi-pulse processing, achieving higher processing accuracy and lower surface damage.

To elucidate the microscopic phase transition behavior of diamond during laser ablation, Raman spectroscopy was performed at the center of the ablated region. The spectra obtained under a pulse duration of 1000 fs with varying single pulse energies are shown in Fig. 5. At a pulse energy of 2 μJ, two distinct features are observed: the characteristic diamond peak at ~1332 cm^{-1} (sp^3 bonding) and an additional broad peak near ~1420 cm^{-1}. The latter is typically attributed to an intermediate response of disordered sp^2 phases, representing a transient amorphous carbon network formed by partial conversion of sp^3 to sp^2 hybridized bonds.

As the laser energy increases, the diamond peak progressively attenuates and nearly vanishes, indicating that the long-range crystal order is destroyed and sp^3 bonds are almost completely broken. Concurrently, the graphitic D band (~1350 cm^{-1}, defect-activated mode) and G band (~1580 cm^{-1}, E_{2g} mode) become increasingly prominent and broaden in width, signifying a transformation of the near-surface region from an sp^3-dominated crystalline state to a disordered sp^2-dominated structure, accompanied by a progressive increase in defect density and lattice disorder.

Additionally, the positions of the Raman peaks exhibit a slight but systematic shift with increasing energy, reflecting the dynamic evolution of the residual stress field. At lower energies, tensile stress dominates, promoting lattice relaxation and triggering localized phase transformation, whereas at higher energies, volumetric ablation and material removal lead to a gradual release of residual stress. The

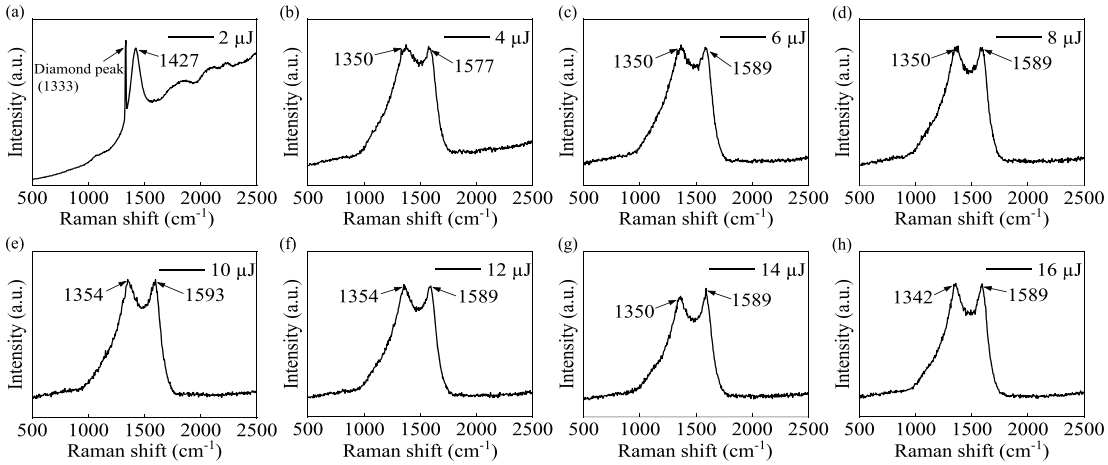

Fig. 5. Comparisons of Raman response curves at different energy densities. This figure presents the Raman spectra of diamond at different energy densities ranging from 2 μJ to 16 μJ. The x-axis represents the Raman shift (cm^{-1}), while the y-axis shows the intensity (a.u.). (a) At 2 μJ, the Raman spectrum reveals a significant peak at 1427 cm^{-1}, which corresponds to the disordered carbon phase, along with the diamond peak at 1333 cm^{-1}, indicating the initiation of material transformation. As the energy density increases to (b) 4 μJ, (c) 6 μJ, and (d) 8 μJ, the diamond peak at 1350 cm^{-1} becomes more prominent, showing the gradual transition from disordered carbon to crystalline diamond. At (e) 10 μJ, (f) 12 μJ, (g) 14 μJ, and (h) 16 μJ, the Raman peaks become sharper, especially at 1350 cm^{-1}, which is associated with the structural modification in the diamond. The 1589 cm^{-1} peak also becomes clearer with increased energy, indicating the presence of amorphous carbon.

continuous increase in the full width at half maximum (FWHM) of all major peaks further indicates a broader distribution of bond lengths and bond angles, characteristic of deepening local disorder and amorphization.

Taken together, these results demonstrate that energy deposition drives a multi-pathway phase transformation of diamond, involving graphitization, amorphization, and the formation of other carbon allotropes. This transformation is governed by the coupled effects of thermal stress accumulation, defect generation, and carbon atomic rearrangement. Once defects form, local lattice relaxation and bond-order reduction favor $sp^3 \rightarrow sp^2$ rehybridization: at moderate peak temperatures and relatively fast cooling rates this yields disordered, amorphous sp^2-rich networks, whereas at elevated energy densities and/or slower local cooling the sp^2 clusters can reorganize into layered graphitic motifs. The competition among peak temperature, stress state, defect density, and cooling kinetics therefore determines whether the dominant outcome is stable amorphization, progressive graphitization, or violent explosive ejection. Importantly, these findings confirm that stress concentration and local lattice relaxation are critical precursors to subsequent material reorganization and carbon phase transformation within the previously proposed "bulging–swelling–melting and recasting–LIPSS formation" evolutionary pathway. However, how the atomic structure gradually evolves cannot be fully resolved by laser experiments alone. Therefore, MD simulations were employed to further elucidate the transient evolution process.

3.2. Atomic damage mechanism driven by energy density

To comprehensively investigate the atomic structural evolution during laser-induced damage of diamond, we conducted MD simulations under three distinct energy densities: 0.1 J/cm^2, 0.12 J/cm^2, and 0.15 J/cm^2, as illustrated in Fig. 6. Our findings reveal that the energy density not only determines the morphology and depth of the amorphous layer but also governs the subsurface phase transition pathways and the material removal mechanisms on the diamond surface.

At a low energy density of 0.1 J/cm^2, the diamond lattice remains largely intact during the initial stages of laser loading (0.2 ps). By 0.6 ps, localized amorphous carbon formation is observed. After the laser pulse ceases (1 ps), an inverted triangular amorphous region emerges on the surface, accompanied by a slight upward bulge. During the subsequent laser unloading phase, this region evolves into a fan-shaped damage zone with a marginally reduced depth. Notably, no atomic ejection or significant material removal occurs, suggesting that the damage at this low energy density is primarily characterized by localized amorphization and the formation of a bulge zone. Similar bulge morphology is also observed from SEM images in Fig. 3.

When the energy density is increased to 0.12 J/cm^2, early damage initiation is observed during the initial loading phase. By 0.6 ps, the formation of amorphous carbon increases. Post-pulse, the damage zone deepens and expands into an inverted triangular geometry, with a more pronounced surface bulge. During the laser unloading phase, localized swelling of carbon atoms upwards occurs. After 51 ps, the amorphous region penetrates deeper into the subsurface, indicating that medium energy density promotes the formation of a localized swelling zone.

At a high energy density of 0.15 J/cm^2, signatures of subsurface phase transitions are evident as early as 0.2 ps. Between 0.6–1 ps, amorphous carbon rapidly expands, forming a deeply penetrating inverted triangular damage zone. Upon unloading, the surface exhibits explosive atomic ejection, with clusters of amorphous carbon atoms migrating outward and undergoing sublimation during the laser unloading phase. This pronounced nonequilibrium evaporation and atomic ejection under high energy input reveals a complex material removal mechanism, driven by ultrafast laser-induced bulge-swelling-blasting processes.

Fig. 7 illustrates the temporal evolution of the temperature field in diamond under laser irradiation at different energy densities (0.1, 0.12, and 0.15 J/cm^2). As shown, the temperature evolution exhibits a characteristic three-stage behavior: rapid heating up, strong nonequilibrium diffusion, and residual heat retention.

During laser loading, the rapid deposition of energy produces highly localized high-temperature zones. At the end of the laser pulse (1 ps), the temperature field exhibits a pronounced spatial gradient, with an extremely high-temperature region concentrated at the laser-irradiated center (exceeding 10,000 K at 0.15 J/cm^2), forming an inverted-conical profile along the depth direction. This morphology highlights the highly localized nature of energy deposition and the dominance of vertical heat conduction. As energy density increases, both the peak temperature and the depth of the heat-affected zone grow significantly: at 0.1 J/cm^2, only a shallow near-surface high-temperature zone forms, whereas at 0.15 J/cm^2, the heat-affected zone penetrates much deeper, demonstrating the critical role of energy density in modulating the magnitude and penetration depth of the thermal field. In the post-

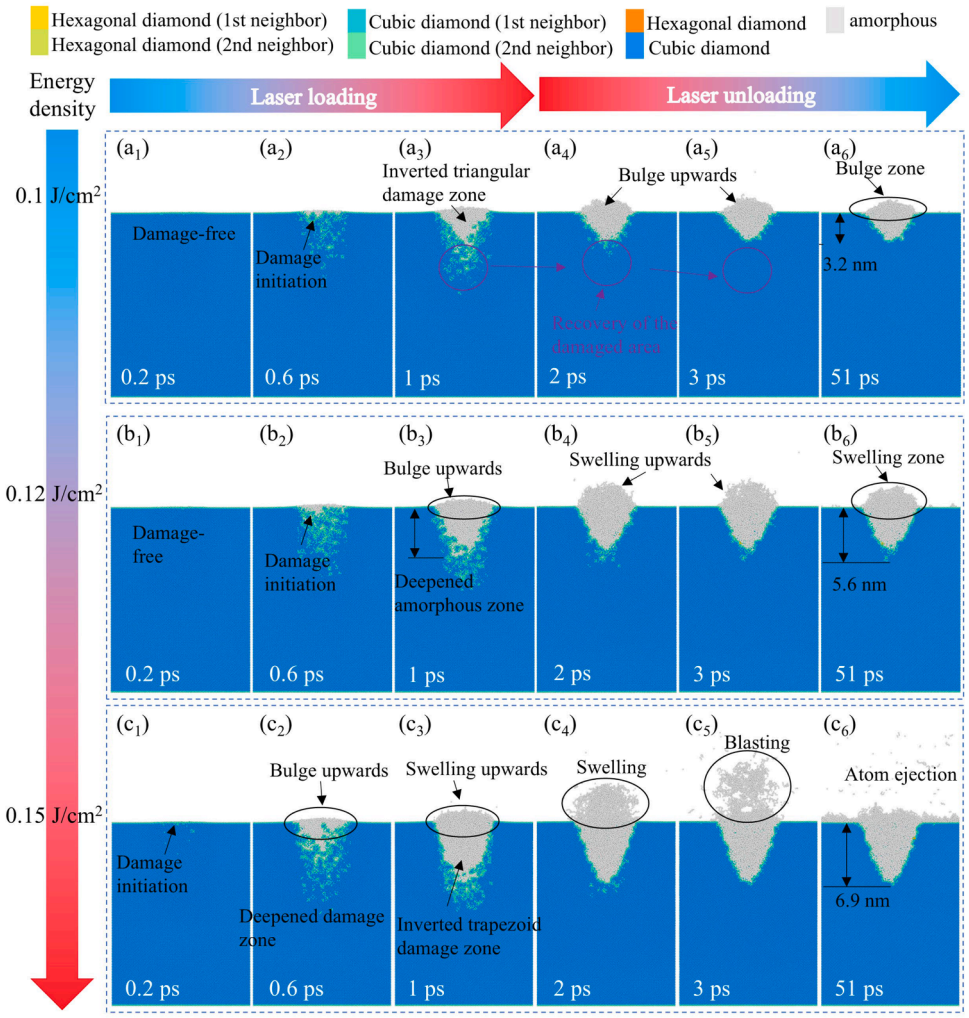

Fig. 6. Energy density-dependent structural evolution of diamond under single-pulse femtosecond laser irradiation at different fluences (0.1, 0.12, and 0.15 J/cm²). Each row corresponds to a specific fluence, while the columns represent different time stages during the laser loading and laser unloading phases. (a_1)-(a_3) Snapshots of structural evolution of diamond during the laser loading phase at the fluence of 0.1 J/cm²: These images show the early stages of the laser-induced deformation in diamond. At 0.1 J/cm², the material initially remains damage-free (a_1), followed by the initiation of damage (a_2). As the laser pulse progresses, an inverted triangular damage zone forms (a_3), indicating localized material transformation. (a_4)-(a_6) Snapshots of structural evolution of diamond during the laser unloading phase at the fluence of 0.1 J/cm²: Following the laser unloading, the damaged region begins to recover (a_4), with the bulge moving upwards (a_5). By 51 ps (a_6), a stable bulge zone with a depth of 3.2 nm has formed, marking the final stage of material deformation. (b_1)-(b_3) Snapshots of structural evolution of diamond during the laser loading phase at the fluence of 0.12 J/cm²: At this fluence, the damage initiation is visible (b_2) followed by the formation of a deep damage zone (b_3), with the material deforming more significantly under the increased laser energy. (b_4)-(b_6) Snapshots of structural evolution of diamond during the laser unloading phase at the fluence of 0.12 J/cm²: During the unloading phase, the bulge continues to expand upwards (b_4), followed by swelling (b_5) and a swelling zone formation (b_6), reaching a depth of 5.6 nm after 51 ps. (c_1)-(c_3) Snapshots of structural evolution of diamond during the laser loading phase at the fluence of 0.15 J/cm²: At the highest fluence (0.15 J/cm²), the damage initiation is more pronounced (c_1), and a deep damage zone forms (c_2). The inverted trapezoid damage zone observed at this stage indicates significant material transformation. (c_4)-(c_6) Snapshots of structural evolution of diamond during the laser unloading phase at the fluence of 0.15 J/cm²: During the unloading phase, swelling occurs at a faster rate (c_4), leading to further material expansion (c_5). After 51 ps, atom ejection is observed (c_6), marking the highest level of material removal with a depth of 6.9 nm.

loading stage (2–3 ps), rapid thermal relaxation occurs alongside nonequilibrium damage formation, leading to a swift decay in surface temperature. However, the damage evolution diverges significantly across energy densities. At low energy (0.1 J/cm²), heat rapidly diffuses and dissipates, with the overall temperature dropping below 3000 K by 3 ps. No significant vaporization or atomic ejection is observed, indicating that damage is dominated by localized amorphization and minor surface reconstruction.

At intermediate energy (0.12 J/cm²), incomplete heat dissipation leaves persistent high-temperature regions in the lattice, resulting in localized atomic vaporization and surface swelling. This reflects a thermos-phase transition coupled damage mechanism, where residual heat drives $sp^3 \rightarrow sp^2$ transitions, accompanied by localized gasification.

At high energy (0.15 J/cm²), the deposited laser energy exceeds the sublimation threshold, maintaining extremely high central temperatures and triggering massive atomic ejection and clustered migration. These processes drive intense sublimation and evaporation, forming deep ablation cater with evident melting-recasting structures, indicative of strongly nonequilibrium thermodynamic material removal mechanisms. By the relaxation stage (50 ps), the low-energy sample's temperature field nearly returns to its initial state, confirming that ultrafast laser irradiation primarily induces reversible surface modification under such conditions. In contrast, the medium- and high-energy samples retain prominent residual thermal damage zones at both the surface and sub-surface. In particular, at 0.15 J/cm², residual heat remains concentrated within the ablation cater regions.

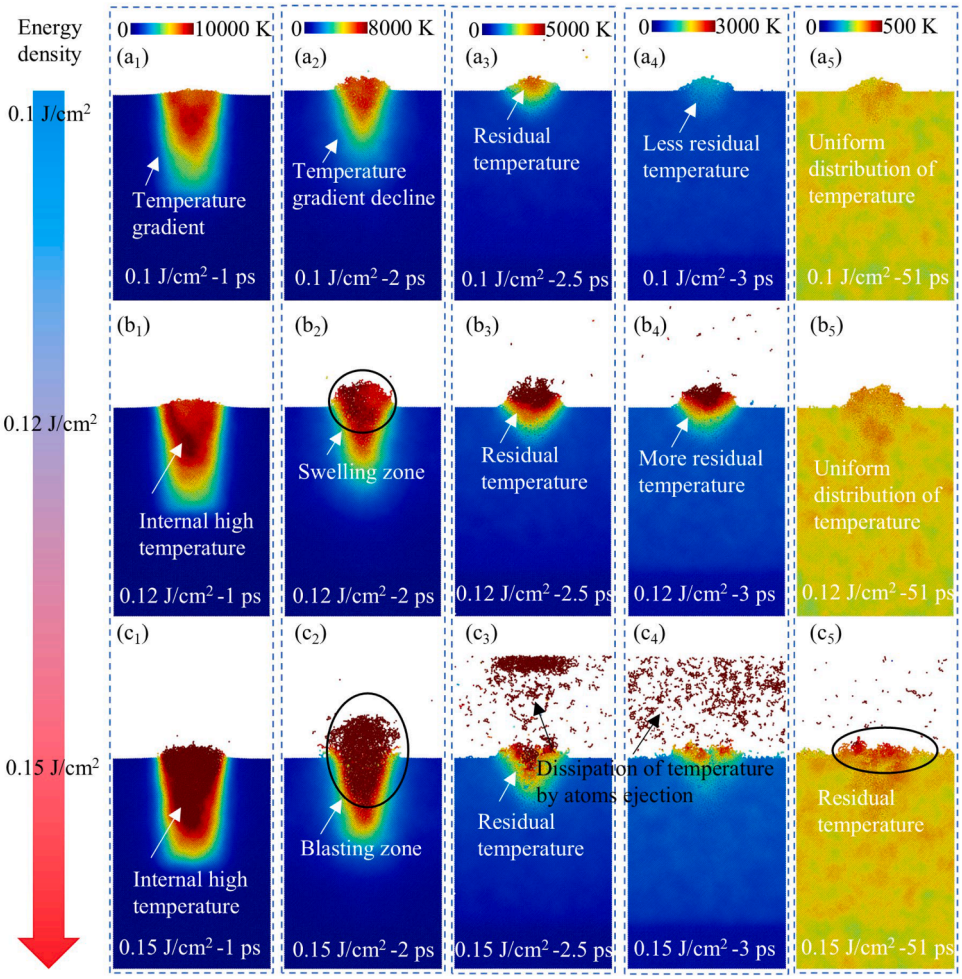

Fig. 7. Temporal evolution of the temperature field in diamond under single pulse femtosecond laser irradiation at different energy densities (0.1, 0.12, and 0.15 J/cm²). The color scale represents the instantaneous temperature distribution from 0 K (blue) to 10 000 K (red), illustrating the thermal response of the material during laser loading, unloading, and relaxation stages. Each row corresponds to a specific laser fluence, while each column shows the evolution at representative times, highlighting the effects of increasing energy density on heating intensity, thermal diffusion, and residual temperature retention. (a) This set of images shows the temperature evolution of diamond under laser irradiation at an energy density of 0.1 J/cm². (a_1) shows the initial temperature gradient formed after 1 ps of laser irradiation, followed by a decline in the gradient (a_2) and residual temperature at 2.5 ps (a_3). At 3 ps, the temperature becomes more evenly distributed (a_4), and after 51 ps (a_5), the temperature is uniformly distributed across the material. (b) The temporal evolution of the temperature field at 0.12 J/cm²: (b_1) shows the internal high temperature at 1 ps. The swelling zone forms by 2 ps (b_2), and the residual temperature is observed at 2.5 ps (b_3). The temperature remains higher, with more residual heat visible at 3 ps (b_4), and the final stage at 51 ps (b_5) shows uniform temperature distribution across the diamond. (c) The temporal evolution of the temperature field at 0.15 J/cm²: (c_1) shows the internal high temperature immediately after laser irradiation. The blasting zone, showing significant material expansion, forms by 2 ps (c_2). By 2.5 ps, residual temperature remains, and at 3 ps (c_3), the temperature dissipates due to atom ejection. The final state at 51 ps (c_5) shows residual temperature around the material, indicating sustained heat effects.

Hydrostatic stress is closely associated with volumetric changes during classical thermodynamic phase transitions in continuous media [99], making it a critical parameter for predicting phase transformation and compression behavior in materials. Therefore, hydrostatic stress was employed to quantify the phase transition and compression response of diamond under laser irradiation. To further elucidate the mechanisms of damage formation and stress regulation in diamond under laser irradiation, we analyzed the temporal evolution of hydrostatic stress at different energy densities (0.1, 0.12, and 0.15 J/cm²), as shown in Fig. 8. The results reveal that laser-induced stress evolutions are governed by energy density, which dictates the stress magnitude, spatial distribution, and damage mode.

At 1 ps after laser loading, the compressive stress at 0.15 J/cm² reaches a peak of 30 GPa, penetrating to the deepest subsurface regions. Moreover, tensile stresses of approximately 15 GPa emerge in the non-irradiated regions of the substrate, indicating that laser energy deposition is not confined to the near-surface zone but instead reconstructs deeper stress fields through rapid stress diffusion. In comparison, the peak compressive stress and penetration depth are significantly reduced at 0.12 J/cm² and 0.1 J/cm², suggesting that lower energy densities only generate localized stress concentrations near the surface. As the system evolves to 2 ps after laser unloading, the compressive stress decays sharply to ~10 GPa, and the tensile stress distribution contracts. However, substantial tensile stress remains concentrated within amorphous regions, indicating that high-pressure/high-temperature conditions drive stress-assisted phase transitions and structural instability. By 50 ps of relaxation, the residual stress distributions exhibit pronounced differences across energy densities. At 0.1 J/cm², nearly all internal stresses are released, with only minor compressive stress remaining. At 0.12 J/cm², stable tensile stresses persist within amorphized regions, while the underlying crystalline substrate retains moderate compressive stresses. In contrast, at 0.15 J/cm², the amorphous damage zone exhibits significantly higher residual tensile stresses, and the deeper substrate maintains strong compressive stresses that are difficult to dissipate. This

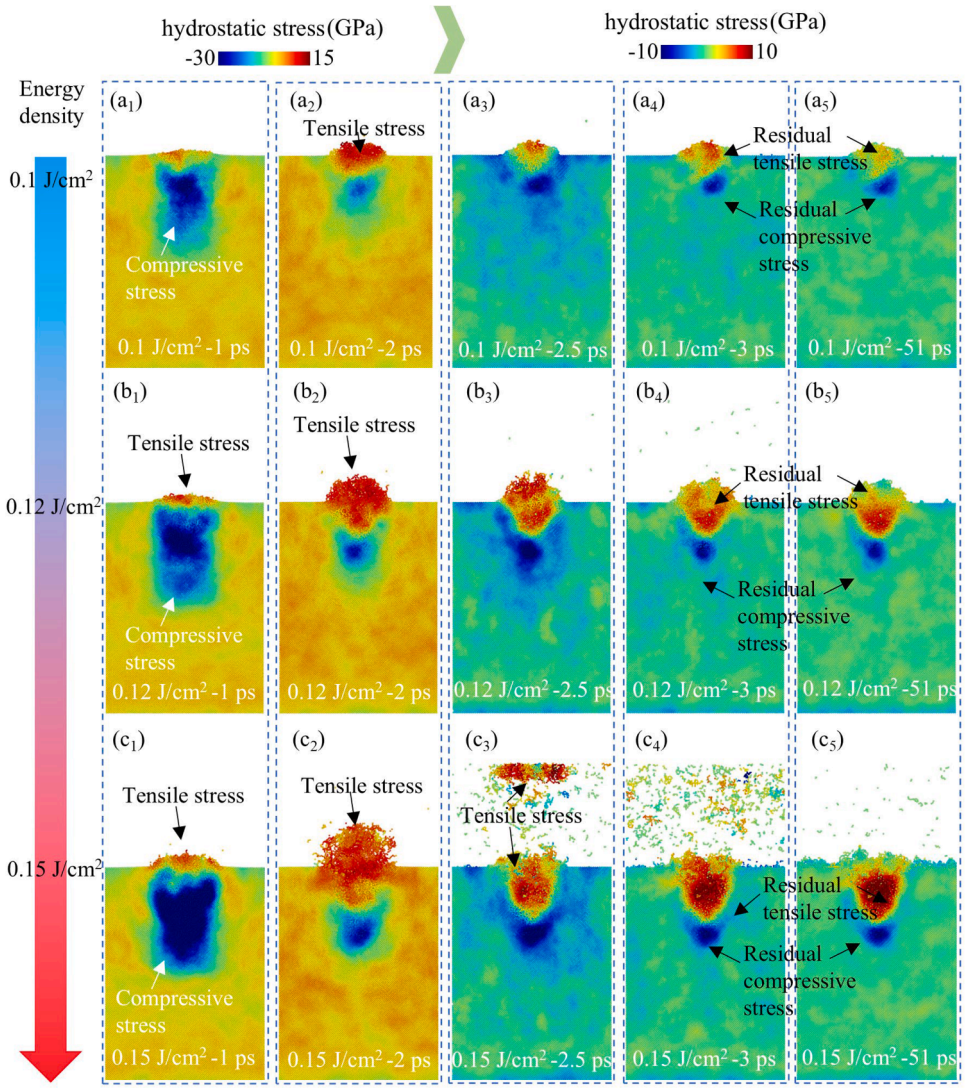

Fig. 8. Temporal evolution of hydrostatic stress in diamond under single pulse femtosecond laser irradiation at different energy densities (0.1, 0.12, and 0.15 J/cm²). The color map represents hydrostatic stress, ranging from −30 GPa (compressive, blue) to +15 GPa (tensile, red) during the laser loading phase, and from −10 GPa to +10 GPa during the unloading and relaxation stages. Each row corresponds to a different laser fluence, while each column shows the evolution of stress at successive times, illustrating the transition from initial compression to relaxation and residual stress formation. (a) This series of snapshots shows the hydrostatic stress distribution during the laser loading and unloading phases at an energy density of 0.1 J/cm². At 1 ps (a_1), compressive stress is observed at the laser impact site. As time progresses, the stress transitions to tensile stress at 2 ps (a_2) and continues to evolve, with the formation of residual tensile stress by 3 ps (a_3). At 51 ps (a_5), the material shows both residual tensile and compressive stress regions, indicating the material's response and recovery after laser unloading. (b) The temporal evolution of hydrostatic stress at 0.12 J/cm²: At an increased energy density of 0.12 J/cm², the material exhibits similar behavior, with tensile stress initiating at 2 ps (b_2). The compressive stress is seen in the early stages (b_1) and transitions into residual tensile and compressive stress regions at later stages, particularly by 51 ps (b_5), showing more pronounced effects of the higher energy density. (c) The temporal evolution of hydrostatic stress at 0.15 J/cm²: the material experiences more intense deformation. Initially, compressive stress is observed at 1 ps (c_1), followed by significant tensile stress at 2 ps (c_2). The stress profile shows further material alteration, including tensile stress and residual compressive stress (c_4). By 51 ps (c_5), both tensile and compressive residual stresses remain, indicating severe material deformation due to the higher energy input.

finding indicates that high energy densities not only increase the depth and extent of damage zones but also freeze long-lived, multiscale residual stress fields.

Integrating the evolution of temperature and stress fields reveals that the core mechanism of ultrafast laser-induced damage is a thermo–stress–phase transition coupled process. High temperatures promote phase transitions, accompanied by volumetric expansion that drives intense compressive stress waves. Stress release and material flow produce alternating tensile–compressive stress distributions at the surface, while ultrafast cooling freezes residual stresses at amorphous–crystalline interfaces, forming long-lived subsurface damage structures. Notably, the residual tensile stresses under high energy density are strongly correlated with phase transitions and plastic deformation and may act as driving forces for subsequent crack initiation and propagation, providing an explanation for the macroscopic ablation pits and surface delamination observed under high-energy irradiation Fig. 9.

At low energy density (0.1 J/cm²), the temperature curve shows a peak below 900 K, dropping rapidly back toward room temperature after pulse termination, indicating a shallow heat-affected zone and rapid thermal recovery during relaxation. At medium energy density (0.12 J/cm²), the corresponding temperature curve reaches nearly 1000 K, while the pressure curve peaks above 2 GPa. Notably, after pulse unloading, the pressure exhibits a secondary rise at around 2 ps, reflecting a transient stress recovery caused by volumetric contraction during phase transformation. This process reveals the strong thermo–stress–phase transformation coupling under ultrafast laser loading: high

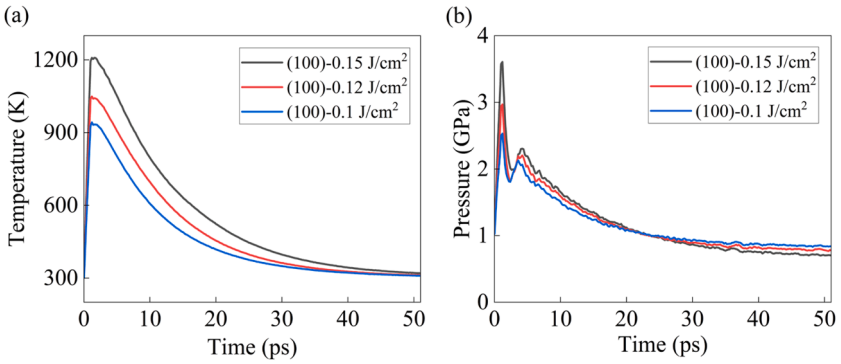

Fig. 9. Comparisons of temperature and pressure during the laser loading and unloading phase. (a) Time series of temperature under different energy densities: This graph shows the temperature evolution for energy densities of 0.1 J/cm², 0.12 J/cm², and 0.15 J/cm². Higher energy densities result in a higher peak temperature and slower cooling rate. (b) Time series of pressure under different energy densities: The pressure increases rapidly during laser loading, with higher energy densities producing higher peak pressures. The pressure then decreases as the material relaxes after unloading.

temperature promotes phase transitions, and the associated abrupt volumetric changes feed back into the local stress field, producing a brief "rebound" in pressure after unloading. At high energy density (0.15 J/cm²), the temperature peak exceeds 1100 K, suggesting that the system

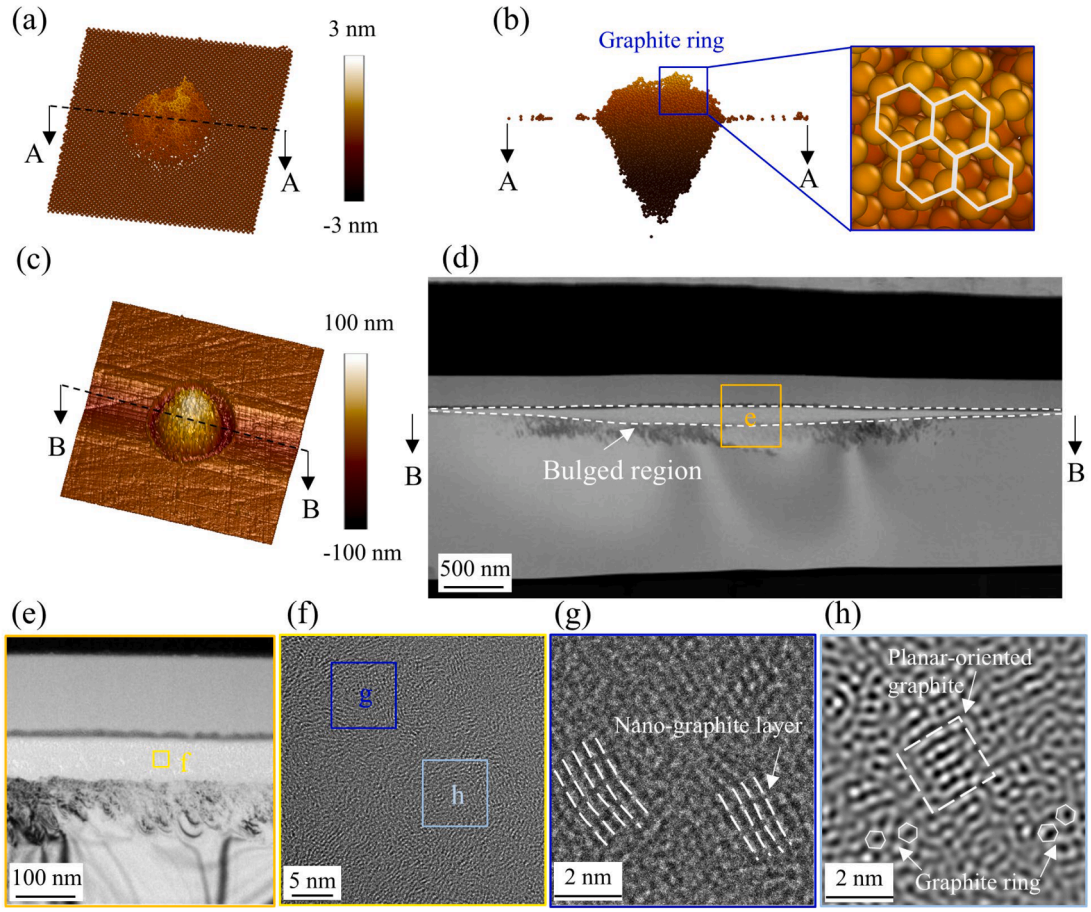

Fig. 10. Analysis of subsurface damage of diamond after single pulse laser. (a) MD snapshots of damage morphology after single-pulse laser simulations. (b) MD snapshots of A-A cross-sectional characterization in (a): The A-A cross-sectional view of the damage morphology from (a) reveals the depth and distribution of the damage, particularly focusing on the changes occurring beneath the surface. (c) AFM image of damage morphology after single-pulse laser experiment, the image shows the deformation caused by the laser and the resulting surface morphology. (d) B-B cross-sectional TEM characterization in (c): The B-B cross-sectional TEM image, taken from (c), shows the subsurface damage, including the bulged region that resulted from the laser impact, providing further insight into the material's response to the laser. (e) Low-magnification TEM image in the bulged region, where material deformation has occurred due to the laser impact. (f) HRTEM images of region e in (d): High-resolution TEM images of the bulged region (region e) from (d) reveal the detailed atomic structure of the damaged area, showing the formation of defects and structural changes. (g) HRTEM images of region g in (f): These images provide a more detailed view of the material's internal structure at a higher resolution, focusing on specific areas where nanostructural changes are observed. (h) HRTEM images of region h in (f): The final set of HRTEM images zooms into the graphite ring and planar-oriented graphite structures, showing the alignment of graphene layers and the transition from diamond to graphite under laser-induced stress.

approaches or even surpasses the local sublimation threshold. The pressure curve shows a pronounced drop and subsequent fluctuations after unloading, reflecting the highly nonequilibrium nature of material removal and stress release processes.

The analysis of the subsurface damage in diamond after a single pulse of laser irradiation is shown in Fig. 10. As illustrated in MD snapshots in Fig. 10(a), laser energy deposition is highly localized to the near-surface region. The lattice structure predominantly retains sp^3 bonding, with only localized sp^2 transitions forming a shallow amorphous layer. The damage is confined to residual surface amorphization, accompanied by slight bulging. The A-A cross-sectional view in Fig. 10(b) reveals the formation of a graphite ring and localized atomic vaporization, indicating significant structural changes. These observations are further confirmed by the AFM morphology in Fig. 10(c), which shows the same bulged structure. Fig. 10(d) presents a transmission electron microscopy (TEM) image of the B-B cross-section of the bulged region in Fig. 10(c). The low-magnification TEM image reveals a pronounced bulged region whose thickness decreases radially towards the periphery. A more magnified view of the bulged region in Fig. 10(e) highlights the complexity of the modified layer, showing a significant structural transformation at the atomic level. High-resolution TEM (HRTEM) images provide direct evidence of the graphite ring formation, as shown in Fig. 10(f). These images confirm that the laser excitation drives the transition from sp^3-bonded diamond to sp^2-rich graphite configurations within the modified layer.

Further detailed HRTEM images in Fig. 10(g) and (h) reveal the

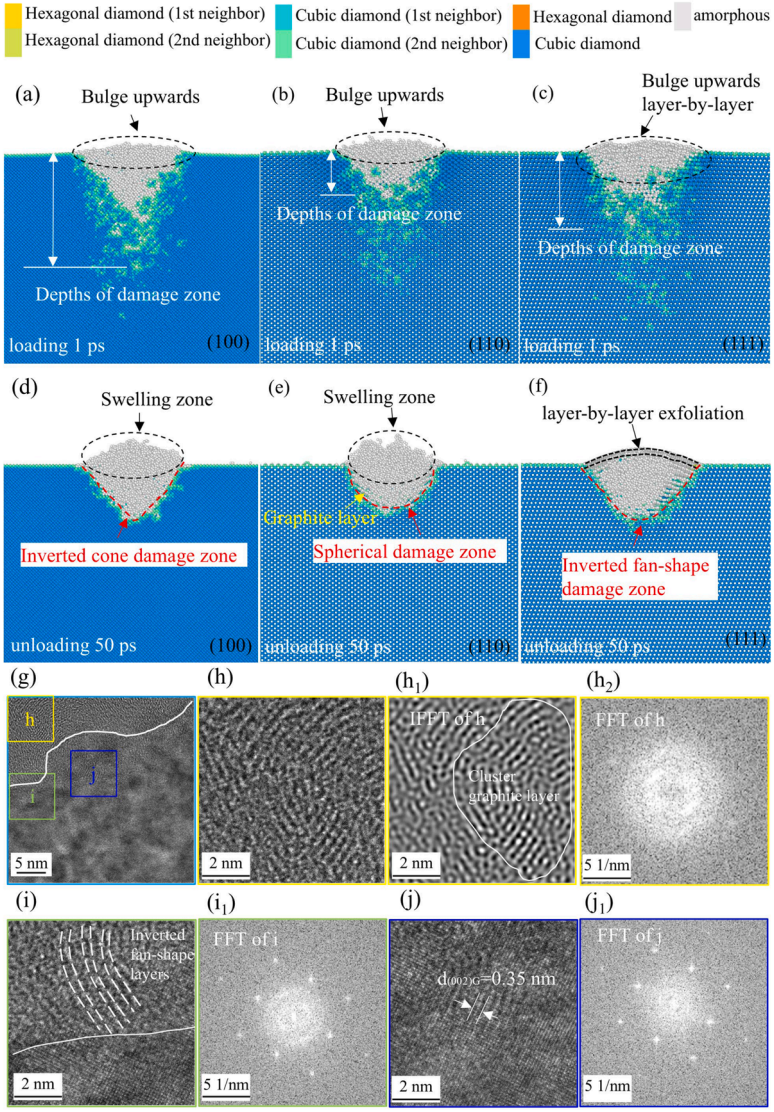

Fig. 11. Crystal orientation-dependent structural evolution of diamond under single pulse laser irradiation. (a) MD snapshots of diamond on the (100) surface after laser loading 1 ps, showing a bulge upwards with a clear depth of damage zone forming. (b) MD snapshots of diamond on the (111) surface after laser loading 1 ps: At the (111) surface, a similar bulging occurs, but with a different depth and distribution of the damage zone, reflecting the surface's distinct crystal orientation. (c) MD snapshots of diamond on the (111) surface after laser loading 1 ps (side view): The (111) surface displays a similar bulging effect with layer-by-layer damage formation. (d) MD snapshots of diamond on the (100) surface after laser unloading 50 ps. (e) MD snapshots of diamond on the (110) surface after laser unloading 50 ps, displaying a similar swelling zone as observed in (d), but with subtle variations in the size and shape of the damage zone, including a more pronounced spherical shape in the damage region. (f) MD snapshots of diamond on the (111) surface after laser unloading 50 ps: the damage zone evolves into an inverted fan-shape, and layer-by-layer exfoliation occurs. (g) HRTEM images of the interface between diamond and the modified layer, showcasing structural changes caused by the laser irradiation. (h) Magnified view of region (g) with IFFT/FFT analyses, revealing the cluster formation of the graphite layer at the interface. (i) Enlarged image of the diamond-modified layer interface with FFT analyses in region (i). (j) Enlarged image of the diamond-modified layer interface with FFT analyses in region (j).

formation of nano-graphite layers and planar-oriented graphite layers, as well as characteristic hexagonal ring motifs. These findings delineate the structural pathway of diamond-to-graphite conversion, showcasing the dynamic evolution of diamond under ultrafast laser irradiation. The transition from a well-ordered sp^3 lattice to disordered graphite regions is evidenced by the formation of a distinct graphite ring, demonstrating the complexity and depth of the laser-induced damage process.

These results reveal a clear mapping between energy density and damage mode. At low energy density, the response is dominated by stable amorphization and residual-stress-driven surface bulging, with essentially no material removal. Medium energy density produces deeper amorphization, the onset of surface graphitization, and more pronounced localized swelling. At high energy density, the system transitions to strong explosive ejection and blasting, marking a shift from confined structural modification to aggressive ablation. Overall, these observations demonstrate that increasing energy density drives the laser–diamond interaction through a progression of regimes, from localized amorphization to coupled graphitization vaporization, and ultimately to violent ablation, each characterized by distinct thermal and stress evolution signatures.

3.3. Atomic damage mechanism driven by crystal orientation

After laser irradiation on the diamond substrate, the laser propagates in all directions within the diamond. Due to the intrinsic anisotropy in the internal atomic structure of diamond, significant differences in damage are observed depending on the crystal orientation. However, these orientation-dependent damage differences are challenging to capture experimentally. In this section, the crystal orientation-dependent damage mechanisms of diamond under single pulse laser irradiation were systematically investigated using MD simulations for three low-index surfaces—(100), (110), and (111).

The snapshots of crystal orientation-dependent structural evolution are shown in Fig. 11. At the laser loading phase (1 ps), as shown in Fig. 11 (a-c), the damage mechanisms vary significantly across different crystal planes. On the (100) surface, a disordered amorphous carbon layer rapidly forms at the surface, while a distinct subsurface phase transition region shaped with an inverted triangular cross-section develops underneath. This results in the deepest amorphous damage zone. Carbon atoms within the laser-affected region migrate upwards, forming a prominent bulging morphology. For the (110) surface, the amorphous layer change is less pronounced, and the surface bulge takes on a shortened inverted triangular cross-section, indicating a more localized response. In contrast, the (111) surface exhibits an inverted fan-shaped damage zone with atomic-layer exfoliation, highlighting the significant anisotropy in structural response.

As laser unloading occurs at 50 ps, as seen in Fig. 11 (d-f), some subsurface damage regions partially recover. The (100) surface shows an inverted cone damage zone, the (110) surface forms a spherical damage zone, and a graphite layer appears at the damage zone interface. For the (111) surface, an inverted fan-shaped damage zone is observed. These results are further supported by the TEM images, which reveal detailed atomic structures at the interface between the pristine substrate and the modified layer.

Fig. 11(g) shows the atomic structure details at the interface between the intact diamond crystal and the damaged region, with white solid lines marking the boundary. The magnified image in Fig. 11(h) and corresponding FFT analyses confirm the formation of clustered graphite layers, evidenced by localized sp^2 fringes and diffraction rings characteristic of nanocrystalline graphite. In Fig. 11(i), the intact diamond lattice gradually transitions into layered protrusions, and the FFT from region (i) reveals the coexistence of diamond and graphite signals, suggesting a heterogeneous phase boundary. Notably, in Fig. 11(j), incipient nano-graphite layers are identified within the diamond lattice, with an interlayer spacing of approximately 0.335 nm corresponding to the (002) planes of graphite. The FFT further demonstrates that the region remains predominantly diamond-like, indicating the nucleation of sp^2 layers within the crystalline matrix.

To investigate the effects of the anisotropy on the subsurface thermal response in diamond under ultrafast laser irradiation, the spatiotemporal evolution of temperature fields for the (100), (110), and (111) crystal surfaces was analyzed under single pulse laser excitation followed by relaxation, as shown in Fig. 12. The results reveal that diamond exhibits a highly localized and ultrafast thermal response under laser excitation, with distinct orientation-dependent anisotropic heat diffusion.

At the onset of laser irradiation, energy is rapidly deposited within the shallow subsurface region, leading to a steep temperature rise exceeding 4000 K in $<$0.5 ps. A pronounced vertical temperature gradient forms, characterized by an extremely hot surface layer and a much cooler underlying matrix. The bulk crystal structure remains largely intact, with the heat strongly localized near the irradiated surface, forming a confined temperature distribution. The (100) surface exhibits the most localized heating due to limited lateral heat conduction, whereas the (110) and (111) surfaces, with higher in-plane thermal conductivities, show more uniform heat distribution across the surface.

As the pulse continues, localized temperatures increase further and surpass 8000 K. This intense thermal excitation weakens the sp^3 bonds in the diamond lattice, triggering sp^2 phase transitions and atomic migration toward the surface. The high-temperature region evolves into a distinctive shape depending on the crystal orientation. On the (100) surface, the heat-affected zone becomes vertically elongated, forming an inverted trapezoidal shape, reflecting limited lateral heat diffusion. In contrast, the (110) and (111) surfaces develop broader, laterally expanded high-temperature zones, with droplet-like morphologies due to their higher in-plane thermal conductivities. This difference highlights the strong anisotropy in heat transport governed by the atomic arrangement in the crystal lattice.

Following the cessation of laser loading, rapid thermal relaxation occurs between 1 and 4 ps. The temperature field contracts quickly, indicating the shallow thermal diffusion characteristic of ultrafast laser processing. However, distinct differences emerge among the three surfaces. The (100) surface, due to its dense vertical atomic packing and lower cross-plane thermal conductivity, demonstrates significant residual heat accumulation near the surface, indicative of thermal trapping and slower cooling. The (110) surface retains elevated surface temperatures in localized regions, with partial heat removal occurring via atom ejection. The (111) surface cools most rapidly, as its layered atomic structure promotes efficient heat dissipation, resulting in minimal residual thermal energy after 4 ps.

These results illustrate the pronounced anisotropy in laser-material interactions, with each crystal surface exhibiting unique thermal response and damage characteristics under the same laser conditions. The (111) surface shows the most efficient heat dissipation and rapid cooling, while the (110) and (100) surfaces exhibit more pronounced thermal trapping and slower relaxation.

To gain deeper insight into the multiscale damage formation mechanisms of diamond under laser processing, the temporal evolution of hydrostatic stress fields across different crystal orientation was systematically analyzed, as illustrated in Fig. 13. The stress evolution process can be divided into three distinct stages: stress initiation (0–0.5 ps), stress region expansion (0.5–1 ps), and stress dissipation (1–51 ps).

During the initial phase of laser pulse irradiation, highly localized energy deposition near the surface leads to a rapid increase in temperature and volumetric strain, establishing a non-equilibrium high-pressure zone. Within 0.5 ps, rapid stress accumulation occurs in the lattice, and high-amplitude stress waves propagate quickly along both normal and radial directions. The spatial distribution of stress is strongly correlated with the laser energy deposition region, revealing the non-equilibrium nucleation mechanism of stress waves under ultrafast energy input. The (100) surface exhibits the most rapid establishment of a high-pressure zone, while the (110) and (111) surfaces show more

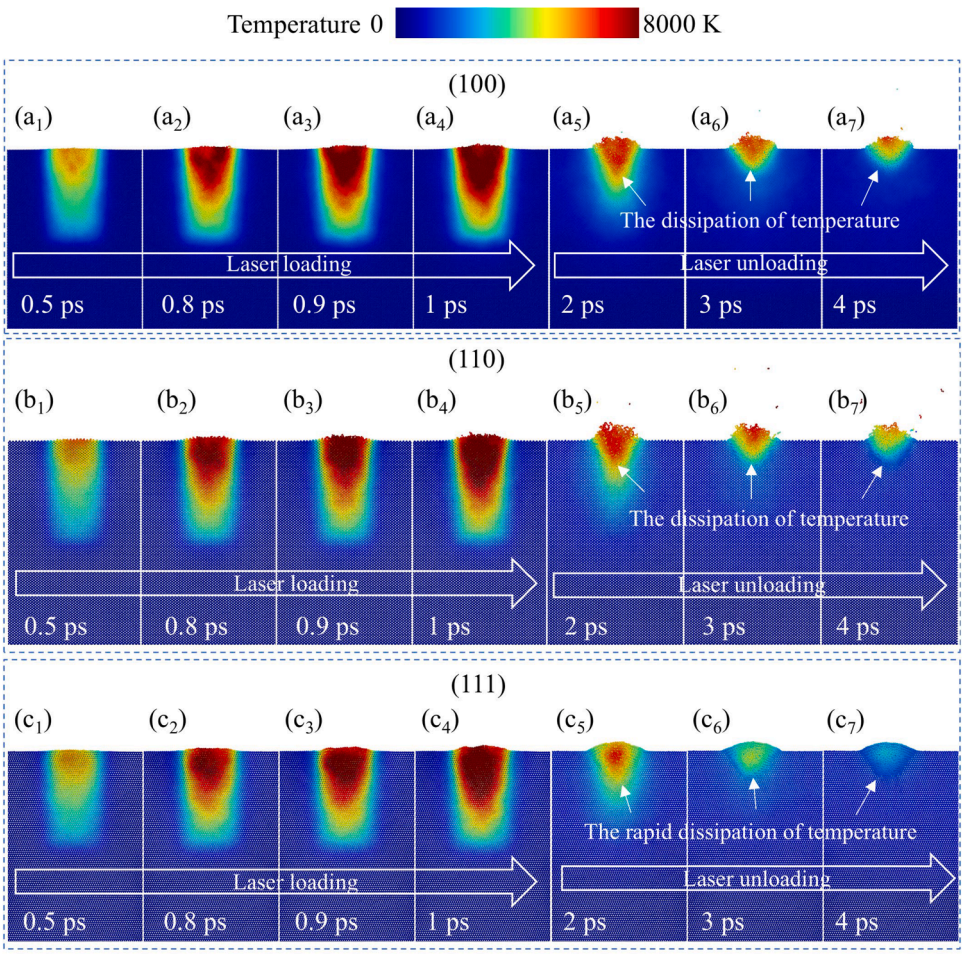

Fig. 12. Spatiotemporal evolution of the temperature field on diamond surfaces with different crystal orientations under single pulse femtosecond laser irradiation at a fluence of 0.1 J/cm². The color scale represents the instantaneous temperature distribution from 0 K (blue) to 8000 K (red). Each subfigure illustrates the temperature evolution at specific time intervals during the laser–matter interaction, revealing both the heating (laser loading) and cooling (laser unloading) stages for different crystallographic surfaces. (a_1)-(a_4) Snapshots of spatiotemporal evolution of the temperature field on the (100) surface during the laser loading phase; (a_5)-(a_7) Snapshots of spatiotemporal evolution of the temperature field on the (100) surface during the laser unloading phase; (b_1)-(b_4) Snapshots of spatiotemporal evolution of the temperature field on the (110) surface during the laser loading phase; (b_5)-(b_7) Snapshots of spatiotemporal evolution of the temperature field on the (110) surface during the laser unloading phase; (c_1)-(c_4) Snapshots of spatiotemporal evolution of the temperature field on the (111) surface during the laser loading phase; (c_5)-(c_7) Snapshots of spatiotemporal evolution of the temperature field on the (111) surface during the laser unloading phase.

gradual stress accumulation due to their higher in-plane thermal conductivities.

Between 0.5–1 ps, the combined action of stress waves and elevated temperatures drives the rapid deepening and lateral expansion of the high-stress region, forming a columnar high-pressure structure. This stage is characterized by multiscale damage mechanisms: (i) the combined effects of high pressure and temperature facilitate the transition, producing amorphous carbon and graphitized products, disrupting the lattice's long-range order; (ii) localized near-surface instability manifests as surface bulging and subsurface swelling, precursors for material removal and surface reconstruction. The (100) surface exhibits the deepest heat-affected zone, forming an inverted cone shape due to limited lateral heat conduction. The (110) and (111) surfaces, with their higher thermal conductivities, show broader high-temperature zones with droplet-like morphologies, reflecting a strong anisotropy in heat transport governed by the atomic arrangement.

The stress evolution and residual stress retention exhibit pronounced crystal orientation dependence. For the (100) plane, a high-pressure zone is rapidly established during stress nucleation, transitioning to tensile stress upon unloading. Despite unloading, significant subsurface compressive residual stress persists at 50 ps, indicating the highest energy retention and residual stress stabilization capability. The (110) plane demonstrates delayed stress expansion relative to (100), with stronger lateral diffusion. Post-unloading, subsurface compressive stress largely dissipates, accompanied by surface carbon atom ejection. The (111) plane shows the slowest stress expansion, with limited lateral spread. The surface exhibits a cyclic compressive-tensile stress response, where stepwise atomic layer bulging serves as a stress-release mechanism. After relaxation, the subsurface transitions predominantly to tensile stress, suggesting more complete stress release.

After laser unloading, rapid thermal relaxation occurs, but high-stress regions remain partially unreleased, especially at crystal-amorphous interfaces and within amorphized zones. Significant compressive residual stress persists up to 51 ps. This residual stress is primarily caused by several factors. First, non-uniform thermal contraction due to ultrafast heating and cooling generates steep temperature gradients, which result in imbalanced thermal shrinkage. Additionally, the elastic mismatch at multiphase interfaces, where differences in elastic modulus and thermal expansion coefficients between diamond, graphite, and amorphous carbon exist, leads to localized residual stress accumulation at these interfaces. Furthermore, defect freezing during rapid solidification traps lattice distortions, contributing to the formation of long-lived residual stress fields.

The orientation-dependent behavior observed in this study can be

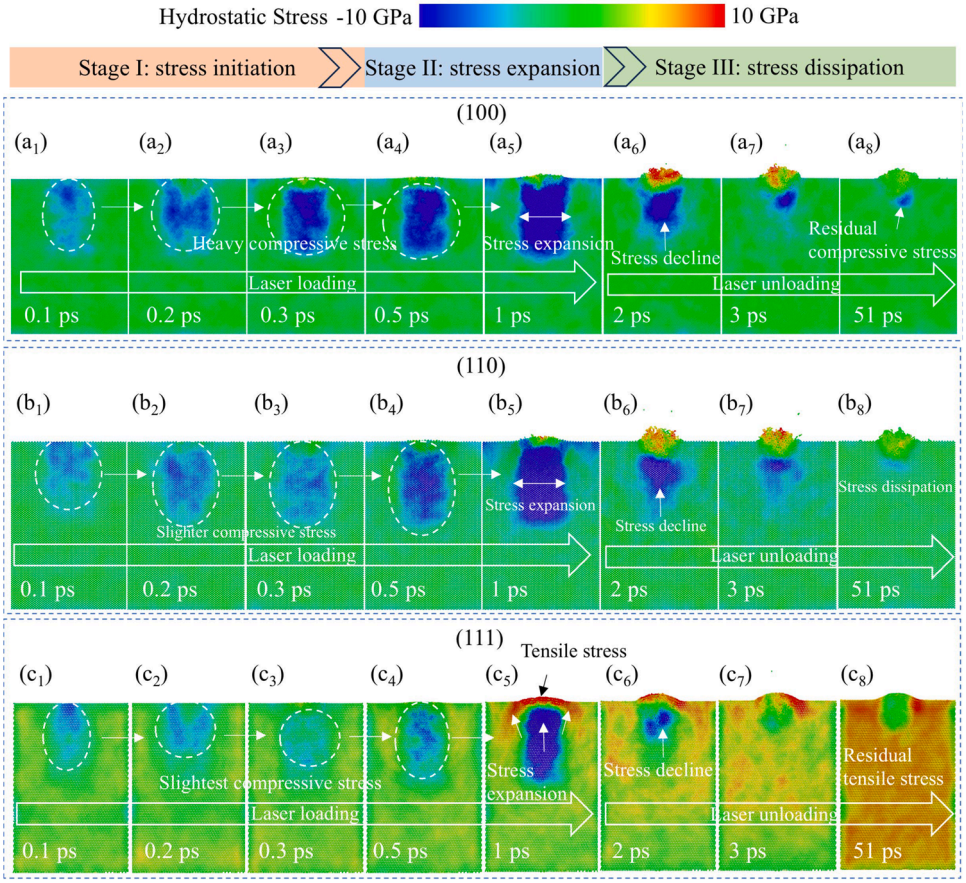

Fig. 13. Spatiotemporal evolution of hydrostatic stress on diamond surfaces with different crystallographic orientations under single pulse femtosecond laser irradiation at a fluence of 0.1 J/cm². The color scale represents hydrostatic stress ranging from −10 GPa (compressive, blue) to +10 GPa (tensile, red). The laser–matter interaction process can be divided into three distinct stages: Stage I – stress initiation, Stage II – stress expansion, and Stage III – stress dissipation. Each subfigure illustrates the stress distribution at representative time intervals during the laser loading and unloading phases. (a_1)-(a_5) Snapshots of evolution process of hydrostatic stress on the (100) surface during the laser loading phase; (a_6)-(a_8) Snapshots of evolution process of hydrostatic stress on the (100) surface during the laser unloading phase; (b_1)-(b_5) Snapshots of evolution process of hydrostatic stress on the (110) surface during the laser loading phase; (b_6)-(b_8) Snapshots of evolution process of hydrostatic stress on the (110) surface during the laser unloading phase; (c_1)-(c_5) Snapshots of evolution process of hydrostatic stress on the (111) surface during the laser loading phase; (c_6)-(c_8) Snapshots of evolution process of hydrostatic stress on the (111) surface during the laser unloading phase.

attributed to the intrinsic atomic arrangements and thermal conduction anisotropy of the diamond lattice. The (100) surface, with its relatively open surface structure and vertical alignment of sp^3 bonds, allows for rapid energy absorption and upward atom migration, promoting amorphization and volumetric expansion. The (110) surface, characterized by asymmetric bonding and lower atomic packing density along the laser incident direction, facilitates localized shear-induced transformations and anisotropic deformation patterns. The (111) surface, with its closely packed atomic planes, acts as a natural template for layered graphitization and inhibits random amorphization, resulting in delayed, yet highly ordered, structural evolution.

The laser-induced temperature rise initiates a cascade of physical responses that couple thermal, mechanical, and structural fields. As the absorbed energy rapidly increases lattice temperature, thermal expansion generates transient compressive stress in the heated zone due to confinement by surrounding colder material. Upon cooling, this stress state gradually evolves into residual tensile stress, especially near free surfaces. The resulting stress redistribution accelerates bond weakening in the heated region, promoting $sp^3 \rightarrow sp^2$ hybridization and amorphization, as well as localized material removal when the tensile stress exceeds the cohesive strength. Therefore, the observed structural transitions are not solely driven by thermal effects but emerge from the synergistic interaction between ultrafast temperature rise, stress accumulation and relaxation, and bond reconfiguration. The orientation-dependent stress evolution highlights the critical role of crystal planes in modulating energy retention, stress release, and structural reconstruction. The higher magnitude and slower relaxation of residual tensile stress in the (100) orientation suggest a greater tendency toward crack initiation, fatigue accumulation, and eventual interfacial delamination under repeated loading or thermal cycling. In contrast, the comparatively more uniform and rapidly dissipated residual stress in the (111) orientation may contribute to improved mechanical stability following laser modification. These results indicate that the stress field evolution is not merely a transient thermal artifact but may directly affect the durability, fracture resistance, and structural reliability of processed diamond components. Therefore, optimizing crystal orientation and energy deposition strategies could be critical for precision laser micromachining where long-term material integrity is required.

4. Conclusions

This study elucidates the atomic-scale damage mechanisms of diamond under femtosecond laser irradiation by integrating systematic experiments with molecular dynamics (MD) simulations. The combined results demonstrate that both energy density and crystal orientation fundamentally govern the damage pathways, ranging from localized amorphization to widespread graphitization and violent ablation. Multi-pulse irradiation produces deep ablation pits through cumulative energy

deposition, whereas single-pulse exposure primarily generates stress-induced surface bulging with minimal material removal.

Experimental characterizations reveal that laser-induced damage in diamond progresses through a sequence of interconnected steps—bulging, swelling, melting/recasting, graphitization, and ablation. These observations establish that the dominant deformation and removal modes are controlled by the interplay of transient thermal spikes, stress-wave dynamics, and rapid bond rearrangement. Higher energy densities promote extensive phase transformations, surface graphitization, and explosive ejection, while lower energy regimes preserve structural continuity and confine the damage to near-surface amorphization.

MD simulations complement and extend the experimental findings by resolving the spatiotemporal coupling between temperature rise, stress-wave propagation, and carbon rehybridization at the atomic scale. The simulations confirm that crystal orientation strongly modulates stress focusing and damage evolution, with (111) planes exhibiting atomic-layer exfoliation and (100)/(110) planes experiencing more rapid stress transmission and pronounced surface deformation. These results demonstrate that laser–diamond interactions are highly anisotropic, shaped by both the crystallographic directionality of stress waves and orientation-dependent phase-transition pathways.

Furthermore, the study establishes that femtosecond laser–induced damage in diamond is governed by a thermo–stress–phase transition coupled mechanism. Stress waves determine the spatial reach of damage propagation, while localized phase transitions and plastic deformation drive structural reconstruction. Residual stresses, inherited from rapid thermal cycling and bond rehybridization, define the persistence and morphology of subsurface damage zones. Importantly, these mechanistic insights reveal that careful tuning of laser parameters—particularly energy density, pulse number, and crystal orientation—offers a viable strategy to minimize subsurface damage, control graphitization, and enhance the precision of micromachining in diamond and other ultra-hard materials.

In summary, this work provides new insights into the mechanisms underlying ultrafast laser-induced damage in diamond, emphasizing the critical influence of energy density and crystal orientation on material removal and structural evolution. In particular, the identified relationships among transient temperature rise, stress evolution, and phase transformation indicate that proper control of pulse energy, pulse accumulation effects, and crystal orientation selection may help suppress deep amorphization and residual stress buildup, thereby minimizing subsurface damage. The findings offer practical guidance for optimizing laser parameters and crystal orientation in precision machining of superhard materials.

CRediT authorship contribution statement

Song Yuan: Writing – review & editing, Writing – original draft, Visualization, Software, Project administration, Methodology, Investigation, Funding acquisition, Formal analysis, Data curation. **Wanxue Zhang:** Writing – review & editing, Formal analysis, Data curation, Conceptualization. **Chi Fai Cheung:** Writing – review & editing, Validation, Supervision, Methodology, Funding acquisition. **Qixian Zhang:** Writing – review & editing, Methodology, Funding acquisition, Formal analysis, Data curation. **Ze Li:** Writing – review & editing, Supervision, Software, Funding acquisition, Formal analysis, Data curation. **Chunjin Wang:** Writing – review & editing, Visualization, Supervision, Software, Resources, Project administration.

Declaration of competing interest

The authors declare that they have no known competing financial interests or personal relationships that could have appeared to influence the work reported in this paper.

Acknowledgements

The authors would like to express thanks to Guangdong Basic and Applied Basic Research Foundation (2025A1515011366), Open Foundation of the State Key Laboratory of Fluid Power and Mechatronic Systems (GZKF-202524), the funding from the Research and Innovation Office of The Hong Kong Polytechnic University (1-W29X, 1-BECE), the National Key R&D Program of China (No. 2023YFE0203800), Innovation and Technology Commission (ITC) of the Government of the HKSAR, China (MHP/151/22). The authors acknowledge the Beijing Super Cloud Computing Center (BSCC) for providing HPC resources that have contributed to the research results reported within this paper.

Data availability

Data will be made available on request.

References

[1] Niu J, Wang J, Sha W, et al. Manufacture and applications of GaN-based piezotronic and piezo-phototronic devices. Int J Extreme Manuf 2024;7(1):012005.
[2] Zhao F, He Y, Huang B, et al. A review of diamond materials and applications in power semiconductor devices. Mater (Basel) 2024;17(14):3437.
[3] Hu X, Ge L, Liu Z, et al. Diamond-SiC composite substrates: a novel strategy as efficient heat sinks for GaN-based devices. Carbon N Y 2024;218:118755.
[4] Cheng Z, Mu F, Yates L, et al. Interfacial thermal conductance across room-temperature-bonded GaN/diamond interfaces for GaN-on-diamond devices. ACS Appl Mater Interfaces 2020;12(7):8376–84.
[5] Li Z, Jiang F, Jiang Z, et al. Energy beam-based direct and assisted polishing techniques for diamond: a review. Int J Extreme Manuf 2024;6(1):012004.
[6] Lu Y, Wang B, Mu Q, et al. Nanoscale smooth and damage-free polycrystalline diamond surface ground by coarse diamond grinding wheel. Diam Relat Mater 2022;125:108971.
[7] Saho E, Hindmarsh S, Sánchez AM, et al. Microcracks in CVD diamond produced by scaife polishing. Diam Relat Mater 2024;144:111008.
[8] Kubota A, Nagae S, Motoyama S. High-precision mechanical polishing method for diamond substrate using micron-sized diamond abrasive grains. Diam Relat Mater 2020;101:107644.
[9] Lu Y, Wang B, Wang Y, et al. Novel surface characteristics observed during grinding of polycrystalline diamond. Appl Surf Sci 2025;684:161883.
[10] Li C, Hu Y, Wei Z, et al. Damage evolution and removal behaviors of GaN crystals involved in double-grits grinding. Int J Extreme Manuf 2024;6(2):025103.
[11] Li C, Wang K, Zakharov O, et al. Damage evolution mechanism and low-damage grinding technology of silicon carbide ceramics. Int J Extreme Manuf 2025;7(2):022015.
[12] Lin J, Hu D, Wang X, et al. The influence of Fenton reaction chemical parameters on the removal of single crystal diamond. Diam Relat Mater 2025;153:112040.
[13] Yuan S, Guo X, Li M, et al. An insight into polishing slurry for high quality and efficiency polishing of diamond. Tribol Int 2022;174:107789.
[14] Liao L, Zhang Z, Meng F, et al. A novel slurry for chemical mechanical polishing of single crystal diamond. Appl Surf Sci 2021;564:150431.
[15] Yuan S, Guo X, Huang J, et al. Sub-nanoscale polishing of single crystal diamond (100) and the chemical behavior of nanoparticles during the polishing process. Diam Relat Mater 2019:100.
[16] Zhu J, Zhao Y, Yuan Z, et al. Mechanism of photocatalysis-assisted chemical mechanical polishing of CVD single crystal diamond. Funct Diam 2025;5(1):2433955.
[17] Yu Z, Zhang Z, Zeng Z, et al. Atomic surface of diamond induced by novel green photocatalytic chemical mechanical polishing with high material removal rate. Int J Extreme Manuf 2024;7(2):025102.
[18] Xiong Q, Lu J, Yan Q, et al. Tribological behavior of single-crystal diamond in a UV photocatalytic-Fenton composite reaction environment. Wear 2024;536-537:205175.
[19] Yuan S, Guo X, Wang H, et al. A theoretical and experimental study on high-efficiency and ultra-low damage machining of diamond. J Manuf Sci Eng 2023;145(7):071006.
[20] Yu J, Liu X, Xu R, et al. Single crystal diamond polishing assisted by inductively coupled plasma etching. Diam Relat Mater 2025:111978.
[21] Xiao Y, Li X, Zhang Y, et al. Highly efficient polishing of polycrystalline diamond via atmosphere inductively coupled plasma. Diam Abras Eng 2024;44(5):553–62.
[22] Liu W, Xiao Y, Zhang Y, et al. Highly efficient and atomic-scale smoothing of single crystal diamond through plasma-based atom-selective etching. Diam Relat Mater 2024;143:110840.
[23] Liu N, Lei L, Jiang H, et al. A highly efficient semi-finishing approach for polycrystalline diamond film via plasma-based anisotropic etching. J Mater Process Technol 2024;332:118578.
[24] Li X, Xiao Y, Wang Y, et al. Microwave plasma-assisted polishing of polycrystalline diamond. Diam Relat Mater 2025;152:111907.

[25] Liu N, Sugimoto K, Yoshitaka N, et al. Effects of polishing pressure and sliding speed on the material removal mechanism of single crystal diamond in plasma-assisted polishing. Diam Relat Mater 2022;124:108899.
[26] Luo H, Ajmal KM, Liu W, et al. Atomic-scale and damage-free polishing of single crystal diamond enhanced by atmospheric pressure inductively coupled plasma. Carbon N Y 2021;182:175–84.
[27] Yuan S, Cheung CF, Shokrani A, et al. Atomic-level flat polishing of polycrystalline diamond by combining plasma modification and chemical mechanical polishing. CIRP Ann 2025;74(1):441–5.
[28] Ye S, Zheng Y, Zhao S, et al. Evolutionary features of subsurface defects of single crystal diamond after dynamic friction polishing. Funct Diam 2024;4(1):2316147.
[29] Yang T, Song D, Hao Z. Progress and prospect of diamond dynamic friction polishing technology. Int J Adv Manuf Technol 2023;124(5):1357–78.
[30] Zheng Y, Cumont AE, Bai M, et al. Smoothing of single crystal diamond by high-speed three-dimensional dynamic friction polishing: optimization and surface bonds evolution mechanism. Int J Refract Met Hard Mater 2021;96:105472.
[31] Liang Y, Zheng Y, Wei J, et al. Effect of grain boundary on polycrystalline diamond polishing by high-speed dynamic friction. Diam Relat Mater 2021;117:108461.
[32] Li C, Wang K, Piao Y, et al. Surface micro-morphology model involved in grinding of GaN crystals driven by strain-rate and abrasive coupling effects. Int J Mach Tools Manuf 2024;201:104197.
[33] Ke J, Liu C, Wang C, et al. Analytical force modeling for laser-assisted diamond machining of brittle materials. Int J Mech Sci 2025:110494.
[34] Li Y, Xing Y, Sun L, et al. Analytical thermal modeling for conventional and in-situ laser assisted turning. Int J Mech Sci 2025;287:109919.
[35] Yuan S, Cheung CF, Fang F, et al. Multi-physical field coupling polishing of diamond for atomic-scale damage-free surface. Int J Extreme Manuf 2026. https://doi.org/10.1088/2631-7990/ae34fb.
[36] Han J, Xin D, Pang J, et al. Laser-assisted manufacturing for sensors. Int J Extreme Manuf 2025;7(4):042008.
[37] Chu W, Wu P, Ye C, et al. Structural color display of polycrystalline diamond processed by femtosecond laser processing. Diam Relat Mater 2025;152:111987.
[38] Zou J, Wang Q, Shen W, et al. Research on the fabrication of high-quality patterned diamond using femtosecond laser. Diam Relat Mater 2024;150:111755.
[39] Liu N, Lei L, Zhu J, et al. An interior damage free approach for nanosecond pulsed laser ablation of single crystal diamond via metal film induced self-maintaining graphitization. J Manuf Process 2024;131:958–72.
[40] Han H, He M, Liu H, et al. Damage evolution and crystalline orientation effects in ultrafast laser micro/nano processing of single-crystal diamond. Opt Laser Technol 2024;169:110120.
[41] Yin J, Chen G, Zhu Z, et al. Ablation mechanism investigation and ablation threshold prediction of single crystal diamond irradiated by femtosecond laser. Diam Relat Mater 2021;111:108173.
[42] Li G, Fan R, Long Y, et al. Material removal mechanism and surface quality in low-fluence femtosecond laser ablation of polycrystalline diamonds. J Mater Process Technol 2025;337:118731.
[43] Wei X, Wen Q, Chen J, et al. Research on gold film-assisted ultraviolet nanosecond laser machining of diamond microgrooves. Opt Laser Technol 2023;158:108793.
[44] Chen N, Wang R, Nagarajan B, et al. Investigation of metal-coating-assisted IR nanosecond pulsed laser ablation of CVD diamond. J Mater Res Technol 2022;18:4114–29.
[45] W P, Butler-Smith, et al. Micro/nanometric investigations of the effects of laser ablation in the generation of micro-tools from solid CVD diamond structures. J Mater Process Technol 2013;213(2):194–200.
[46] C MPAB, A MB, C BKA, et al. Impulse laser cutting of diamond accompanied by phase transitions to fullerene-type onions. Diam Relat Mater 2021;113:108281.
[47] Luo Z, Lu J, Wu L, et al. Study on the material removal characteristics of single crystal diamond polished by infrared picosecond laser. Int J Refract Met Hard Mater 2025;132:107275.
[48] Xu F, Hu, et al. Numerical analysis of Nd:YAG pulsed laser polishing CVD self-standing diamond film. Chin J Mech Eng 2013;26(1):121–7.
[49] Liu H, Xie L, Lin W, et al. Optical quality laser polishing of CVD diamond by UV pulsed laser irradiation. Adv Opt Mater 2021;9(21):2100537.
[50] Zhang Z, Zhang Q, Xu J. The crack propagation and surface formation mechanism of single crystalline diamond by a nanosecond pulsed laser. J Appl Phys 2021;(11):130.
[51] Konov VI. Laser in micro and nanoprocessing of diamond materials. Laser Photon Rev 2012;6(6):739–66.
[52] Wang L, Chen X, Wu G, et al. Study on site-specific polishing of polycrystalline diamond film by KrF excimer laser. J Laser Micro Nanoeng 2017;12(2):62.
[53] Zhang Q, XU B, Li J, et al. Experimental study of nanosecond laser ablation mechanism and polishing of CVD diamond. Infrared Laser Eng 2024;53(10):1–13.
[54] Takayama N, Yan J. Mechanisms of micro-groove formation on single-crystal diamond by a nanosecond pulsed laser. J Mater Process Technol 2017;243:299–311.
[55] Xing Y, Liu L, Hao X, et al. Micro-channels machining on polycrystalline diamond by nanosecond laser. Opt Laser Technol 2018;108:333–45.
[56] Kononenko TV, Pivovarov PA, Khomich AA, et al. Processing of polycrystalline diamond surface by IR laser pulses without interior damage. Opt Laser Technol 2019;117:87–93.
[57] Kononenko TVP, Khomich PA, Khmelnitskii AA, Konov RA, I V. Effect of absorbing coating on ablation of diamond by IR laser pulses. Quantum Elec (Woodbury) 2018;48(3).
[58] Ali B, Litvinyuk IV, Rybachuk M. Femtosecond laser micromachining of diamond: current research status, applications and challenges. Carbon N Y 2021;179:209–26.
[59] Wang H, Wen Q, Xu X, et al. Ablation characteristics and material removal mechanisms of a single-crystal diamond processed by nanosecond or picosecond lasers. Opt Express 2021;29(14):22714–31.
[60] Prieske M, Vollertsen F. Picosecond-laser polishing of CVD-diamond coatings without graphite formation. Mater Today: Proc 2021;40:1–4.
[61] Zhai J, Zhang Q, Zhu Y. Picosecond laser ablation of polycrystalline CVD diamond. Opt Laser Technol 2022;155:108403.
[62] Pimenov SM, Vlasov II, Khomich AA, et al. Picosecond-laser-induced structural modifications in the bulk of single-crystal diamond. Appl Phys A 2011;105:673–7.
[63] Yan B, Chen N, He N, et al. Surface modeling and component analysis of picosecond laser ablation of CVD diamond. Diam Relat Mater 2021;111:108191.
[64] Okamoto Y, Okada A, Kajitani A, et al. High surface quality micro machining of monocrystalline diamond by picosecond pulsed laser. CIRP Ann 2019;68(1):197–200.
[65] Meshram T, Yan J. Formation of laser-induced periodic surface structures on reaction-bonded silicon carbide by femtosecond pulsed laser irradiation. Nanomanufacturing Metrol 2023;6(1):4.
[66] Zhou Z, Xu Z, Song Y, et al. Silicon vacancy color centers in 6H-SiC fabricated by femtosecond laser direct writing. Nanomanufacturing Metrol 2023;6(1):7.
[67] Han H, Liu H, Huang J, et al. Atomic-level insight into sequential evolution of nanocomposite carbon structures in femtosecond laser processing of diamond. Int J Mach Tools Manuf 2025;206:104247.
[68] Yan B, He N, Chen N, et al. Achieving precise graphenization of diamond coatings below the interfacial thermal stress threshold. Int J Extreme Manuf 2025;7(1):015106.
[69] Wei C, Ma Y, Han Y, et al. Study on femtosecond laser processing characteristics of nano-crystalline CVD diamond coating. Appl Sci 2019;9(20):4273.
[70] Boerner P, Hajri M, Ackerl N, et al. Experimental and theoretical investigation of ultrashort pulsed laser ablation of diamond. J Laser Appl 2019;(2):31.
[71] Michael K, Greiner L, Dreizehnter P, et al. Ultra-short pulsed laser processing of single crystalline diamonds for tooling applications. J Laser Appl 2023;35(4).
[72] Dongming G. High-performance manufacturing. Int J Extreme Manuf 2024;6(6):060201.
[73] Zhang Z, Zhang Q, Wang Q, et al. Investigation on the material removal behavior of single crystal diamond by infrared nanosecond pulsed laser ablation. Opt Laser Technol 2020;126:106086.
[74] Fang F. On the three paradigms of manufacturing advancement. Nanomanufacturing Metrol 2023;6(1):35.
[75] He X, Chen R, Xie J. Anisotropic ablation mechanism of single crystal diamond surface in ultrafast laser processing: a molecular dynamics study. Opt Laser Technol 2025;190:113171.
[76] Liu J, Wu M, Sun Z, et al. The picosecond laser ablation mechanism of monocrystalline silicon by coupling two-temperature model (TTM)-molecular dynamic (MD). Appl Surf Sci 2024;661:160022.
[77] Li C, Hu Y, Zhang F, et al. Molecular dynamics simulation of laser assisted grinding of GaN crystals. Int J Mech Sci 2023;239:107856.
[78] He Y, Xiao G, Liu Z, et al. Subsurface damage in laser-assisted machining titanium alloys. Int J Mech Sci 2023;258:108576.
[79] Du X, Shuang S, Zhao J, et al. Extra strengthening and Bauschinger effect in gradient high-entropy alloy: a molecular dynamics study. Int J Mech Sci 2024;264:108829.
[80] Liu J, Liang S, Zhu Y, et al. Molecular dynamics simulations informed hyperelastic constitutive model with insights into entangled free chains. Int J Mech Sci 2024;280:109542.
[81] Dai L, Li Y, Luo W, et al. Effect of micro-diamond and nano-polycrystalline diamond interfacial microstructure on OLC phase transition. Chem Eng J 2024;497:155613.
[82] Goh B, Choi J. Geometric formulation of residual stress propagation in diamond lattice substrate. Int J Mech Sci 2025:110566.
[83] Peng K, Huang H, Xu H, et al. A molecular dynamics study of laser melting of densely packed stainless steel powders. Int J Mech Sci 2023;243:108034.
[84] Zhao J, Li W, Chen S, et al. Atomic-scale material removal and deformation mechanism in nanoscratching GaN. Int J Mech Sci 2025;285:109804.
[85] Zhao J, Zhang C, Liu F, et al. Understanding femtosecond laser internal scribing of diamond by atomic simulation: phase transition, structure and property. Carbon N Y 2021;175(2):352–63.
[86] Tian B, Ma W, Chen S, et al. Effects of pulsed laser processing on structural evolution of diamonds - A molecular dynamics and experimental study. Int J Refract Met Hard Mater 2024;119:106560.
[87] Shi Y, Chen Z, Yang H, et al. Micro-to nano-scale topographical etching of diamond substrate via anisotropically atomic removal. Appl Surf Sci 2024;655:159589.
[88] Zelenina A, Smirnov N, Pakholchuk P, et al. High-temperature multi-vacancy mediated diffusion of nitrogen in diamond: MD simulations and mid-IR laser experiments. Diam Relat Mater 2024;148:111427.
[89] Li C, Liu G, Gao C, et al. Atomic-scale understanding of graphene oxide lubrication-assisted grinding of GaN crystals. Int J Mech Sci 2025;286:109934.
[90] Wang K, Chen H, Wu Y, et al. Brittle-to-ductile transition depth and ductile deformation mechanisms during grinding of 4H-SiC crystals. Tribol Int 2025:110972.
[91] Aktulga HM, Fogarty JC, Pandit SA, et al. Parallel reactive molecular dynamics: numerical methods and algorithmic techniques. Parallel Comput 2012;38(4–5):245–59.
[92] Plimpton S. Fast parallel algorithms for short-range molecular dynamics. J Comput Phys 1995;117(1):1–19.
[93] Stukowski A. Visualization and analysis of atomistic simulation data with OVITO-the Open Visualization Tool. Model simul mater sci eng 2009;18(1):015012.

[94] Pastor RW, Brooks BR, Szabo A. An analysis of the accuracy of Langevin and molecular dynamics algorithms. Mol Phys 1988;65(6):1409–19.
[95] Tersoff J. Modeling solid-state chemistry: interatomic potentials for multicomponent systems. Phys rev B 1989;39(8):5566.
[96] Batcho PF, Schlick T. Special stability advantages of position-Verlet over velocity-Verlet in multiple-time step integration. J Chem Phys 2001;115(9):4019–29.
[97] Li ZQ, Wang J, Wu Q. Molecular dynamics simulation of the ablation process in ultrashort pulsed laser machining of polycrystalline diamond. Adv Mat Res 2012; 500:351–6.
[98] Li ZQ, Wang J, Sun T. Atomistic simulations of ultrashort pulsed laser ablation of polycrystalline diamond. Curr Nanosci 2013;9(6):804–11.
[99] Cross LWGraham. Silicon nanoparticles: isolation leads to change. Nat Nanotechnol 2011;6(8):467.